OPEN ACCESS

The Relation Between the Microstructure of Aluminum Alloy 7075-T6 and the Type of Cerium Salt in the Formation of the Cerium Conversion Layer

To cite this article: Ingrid Milošev *et al* 2022 *J. Electrochem. Soc.* **169** 091501

Journal of The Electrochemical Society, 2022 **169** 091501

The Relation Between the Microstructure of Aluminum Alloy 7075-T6 and the Type of Cerium Salt in the Formation of the Cerium Conversion Layer

Ingrid Milošev,[*,z] **Barbara Kapun, and Peter Rodič**

Jožef Stefan Institute, Department of Physical and Organic Chemistry, Jamova c. 39, SI-1000 Ljubljana, Slovenia

The deposition of the cerium conversion layer on aluminum alloy 7075-T6 proceeds by a simple procedure of immersion, but it is affected by several factors which govern its corrosion protectiveness. The study aimed to investigate two crucial relationships: (i) how the type of cerium salt used for conversion affects the composition, thickness, and electrochemical characteristics of the deposited layers, and (ii) how the deposition depends on the type of intermetallic particles. Four sets of samples were prepared by immersion in 0.1 M NaCl with and without adding 3 mM Ce(III) salts: chloride, nitrate, and acetate. Samples were analyzed by scanning electron microscopy with chemical analysis at the same site before and after immersion. Therefore, this study is site-specific and targets the mode of corrosion and deposition of the Ce-conversion layer as a function of the intermetallic particle's type. The type of anion of Ce salt affects the path of conversion layer formation. The corrosion protectiveness is the highest for acetate salt. The model was postulated, describing the precipitation of a mixed layer by the dynamic "two-way road" process of selectively dissolving elements from the substrate and precipitating Ce-hydroxide. Dealloying of intermetallic particles is the governing mechanism for the precipitation of large Ce-containing deposits.
 [DOI: 10.1149/1945-7111/ac8d35]

Manuscript submitted July 19, 2022; revised manuscript received August 25, 2022. Published September 7, 2022.

Supplementary material for this article is available online

The conversion of cerium ions from the solution to form the precipitated layer of Ce(III)-hydroxide at the metal sample has been a known method of corrosion protection for almost 40 years. Hinton et al. reported that Ce-hydroxide progressively replaced Al oxide during 20 days of immersion on aluminum alloy (AA) 7075-T6 in 200 ppm $CeCl_3$ solution.[1,2] Chemically, the Ce-conversion layer is hardly soluble and protects the underlying substrate by excluding its contact with a corrosive medium. Sometimes these coatings are also referred to as interphase inhibitors. Electrochemically, the action of the Ce-conversion layer is primarily on the cathodic reaction, i.e. it decreases the kinetics of oxygen reduction reaction[a].[1–3] The deposition proceeds primarily at the intermetallic particles (IMPs), the sites at which cathodic reaction occurs in aluminum alloys.[1–4] The cathodic reaction produces an increased concentration of OH^- ions[a], leading to local alkalinization up to pH 8.5 required for the precipitation of dissolved Ce(III) ions together with OH^- ions to form Ce(III)-hydroxide at the metal surface.[5] This process can be generally presented as

$$Ce^{3+}_{(aq)} + 3OH^-_{(aq)} \rightarrow Ce(OH)_{3,(s)}, \quad [1]$$

keeping in mind that the mechanism is complex and includes intermediates.[6] With prolonged immersion, deposition occurs at the matrix as well.[4] This process is thus a pH-driven process that initiates at the cathodic "islands" and then spreads over the matrix with prolonged immersion. Oxygen dissolved in an aqueous solution is the source of hydroxyl ions[a] required for the precipitation; this is referred to as non-accelerated conversion and is a relatively long-lasting process, which may take hours or days for the layer to fully developed. Adding oxidants such as hydrogen peroxide results in the more intensive formation of OH^- ions, resulting in the shortening of conversion time.[5] The mechanism of pH-driven precipitation and substrate protection by deposition Ce(III)-hydroxide at the surface has been demonstrated not only on AA7075-T6 but also on other aluminum alloys such as AA2024-T3.[7]

The deposition mechanism is relatively well investigated, especially for Cu-containing alloy AA2024-T3.[4,8–10] In addition to $CeCl_3$,[1–4,9] several other Ce(III) salts have been used to deposit conversion layers, including, for example, Ce(III) nitrate,[10–12] Ce(III) diphenyl phosphate,[13] and Ce(III) cinnamate.[14]

In contrast, comparative studies on AA7075-T6 are more scarce.[1,2,15] Literature reports reveal that the type of salt affects the deposition path, but the mechanism is not yet fully understood. In our previous studies, we have addressed the effect of Ce salt on the protective mechanism of deposited conversion layers on AA7075-T6 and AA2024-T3 and reported that different Ce (III) salts act differently; moreover, their action on different Al alloys is not the same but is mainly dependent on the composition of the substrate.[16–20] The latter is, of course, determined by the type and composition of IMPs. The Ce-conversion layer deposited on AA7075-T6 immersed in an aqueous solution of $CeCl_3$ acts like a typical cathodic inhibitor shifting the corrosion potential in the negative direction and decreasing cathodic current density.[16–18] Similar action was observed for Ce(III) acetate.[16,17,20] In contrast, Ce(III) nitrate produces the conversion layer, acting as an anodic inhibitor.[17,18] The protective action also depends on the immersion time: it may change from cathodic to anodic type, related to the progressive surface coverage and redistribution of cathodic and anodic activities.[17] Ce(III) acetate was established as an effective inhibitor that followed a different path than chloride and nitrate salts forming the layer that could re-passivate in a chloride medium.[16,17] Other organic cerium salts than acetate show a similar inhibitory path, such as Ce-formate and Ce-propionate; among them, the latter was the most efficient inhibitor.[21]

On AA7075-T6, deposition of Ce(III)-hydroxide from both Ce(III) chloride and nitrate was detected primarily on the Al(Fe,Cu)-containing IMPs.[1,17–19] On AA2024-T3, deposition was related mainly to Cu-containing IMPs, primarily Al_2CuMg (S-phase).[4,9,22] It is now well established that upon immersion of AA2024-T3 in chloride solution S-phase undergoes a transition from being electrochemically anodic IMPs relative to the matrix to a nobler (cathodic) character. The reason is the selective dissolution of Mg and partially Al which results in the enrichment of IMP in Cu remnants, as first proposed by Buchheit et al.[23,24] The Cu-enriched IMP becomes a strong cathode, and the site where the local pH rapidly increases[a] to the level required for the

*Electrochemical Society Member.
[z]E-mail: ingrid.milosev@ijs.si

[a]$O_2 + 2H_2O + 4e^- \rightarrow 4OH^-$ and $O_2 + 2H_2O + 2e^- \rightarrow H_2O_2 + 2OH^-$

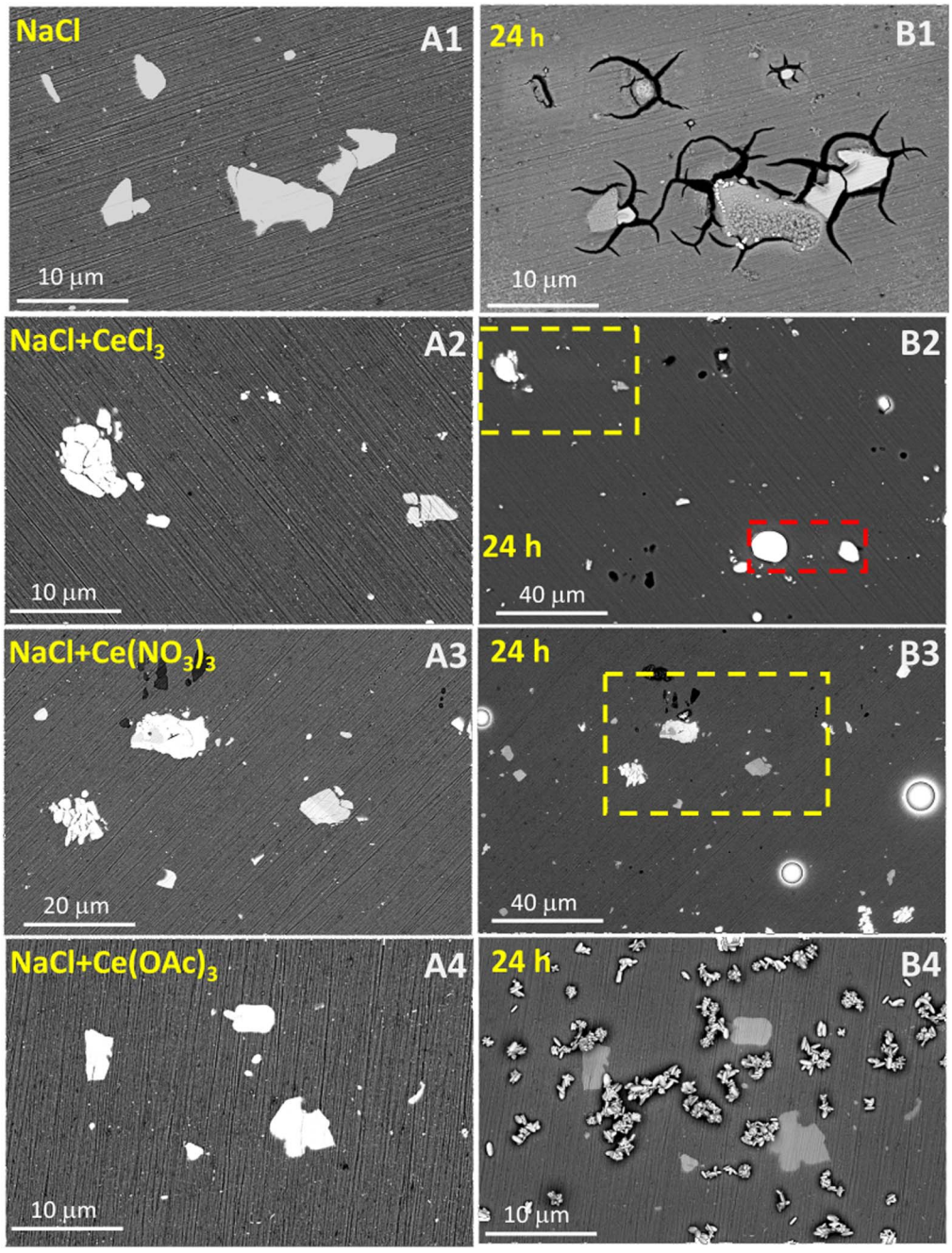

Figure 1. SEM images taken of the AA7075-T6 samples before and after immersion for 24 h in (A1, B1) 0.1 M NaCl, (A2, B2) 0.1 M NaCl + 3 mM $CeCl_3$, (A3, B3) 0.1 M NaCl + 3 mM $Ce(NO_3)_3$, and (A4, B4) 0.1 M NaCl + 3 mM $Ce(OAc)_3$. The analysis was made at the same site before and after immersion in the electrolyte. For samples B2 and B3, the area investigated after immersion was expanded to account for larger deposits formed somewhat outside the area analyzed before immersion (denoted by the yellow rectangle). The red rectangle in B2 denotes the area where the FIB cross-section analysis was made (Figs. 15 −18). Images were taken in BSE mode at 5 kV.

deposition of Ce(III)-hydroxide.[4,9,22] The exact relation between Ce-conversion and alloy microstructure, however, remains to be elucidated and deserves further attention, especially in the light of recent investigations of local corrosion processes on IMPs, emphasizing the importance of dealloying of other IMPs than the S-phase, i.e. Al(Fe,Cu)Si intermetallic particles,[25–29] and even Mg_2Si.[25,30] Dealloying of IMPs (Al_2CuMg, Al_2Cu, Al_7Cu_2-Fe(Mn), and $Al_{76}Cu_6Fe_7Mn_5Si_6$) was reported to be the main factor governing the rate of Ce precipitation in AA2024-T3 when immersed in NaCl containing $Ce(NO_3)_3$.[31] The preferential heavy deposition of the Ce-conversion layer formed by conversion of $Ce(NO_3)_3$ salt on very active Cu-rich IMPs was also demonstrated on cast Al-Si alloy.[32] The use of analytical techniques such as cross-sectional transmission electron microscopy (TEM)[27,28,31] and focus ion beam (FIB) scanning electron microscopy (SEM) with energy-dispersive X-ray spectroscopy (EDS), along with localized techniques such as scanning Kelvin probe force microscopy (SKPFM)[25,32] was crucial to demonstrate dealloying of IMPs.

In the context of recent reports[31,32] and taking into account that several points of the mechanism of Ce-hydroxide deposition remain to be elucidated in more detail, we aimed to investigate more closely the relationship between the type of Ce(III) salt added to produce the conversion layer and type of Al alloys

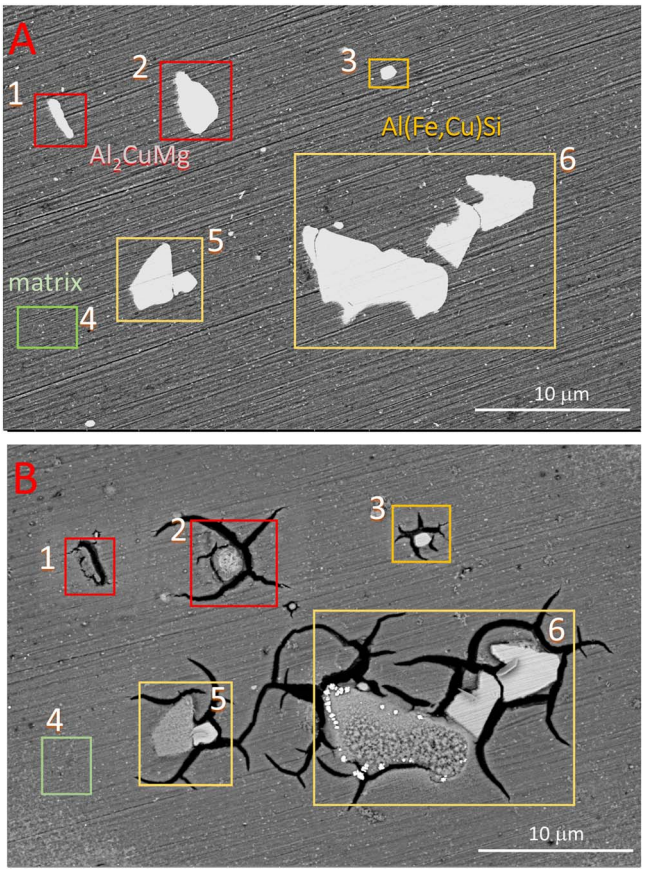

Figure 2. SEM images taken of the AA7075-T6 sample before (A) and after (B) immersion for 24 h in 0.1 M NaCl. The analysis was made at the same site before and after immersion in the electrolyte (Figs. 1A1, 1B1). The compositions of the sites denoted at SEM images by numerals 1–6 were analyzed by EDS. EDS composition in wt% is presented as pie graphs in Fig. 3. The green rectangle denotes the matrix, red rectangles denote Al-Cu-Mg (S-phase) IMP, and yellow rectangles denote Al(Fe-Cu)-based IMPs. SEM images were taken in BSE mode at 5 kV.

substrate, i.e. type of IMPs. To this end, we designed a relatively simple experiment: AA7075-T6 samples were immersed for 24 h in 0.1 M NaCl with 3 mM Ce(III) salts: $CeCl_3$, $Ce(NO_3)_3$ and $Ce(CH_3COO)_3$ (denoted as $Ce(OAc)_3$) under non-accelerated conditions and non-modified pH. For reference, a set of samples was prepared in NaCl solution. Prepared sets of samples were then subject to (i) FIB/SEM/EDS analysis to address the morphology and composition of the surface and (ii) electrochemical measurements in NaCl solution to address the protection mechanism. Before and after preparation, samples were analyzed by FIB/SEM/EDS at the same site. Therefore, this study is site-specific and accounts for the mode of corrosion and layer deposition as a function of the intermetallic particle's type. The investigation of the same IMP site before and after immersion is crucial to account for the relationship between Ce-conversion layer deposition and microstructure, especially for aluminum alloys, a heterogeneous system with thousands of IMPs of different compositions.[33] Similar studies, performed at the same site before and after immersion, contributed valuable information on the mechanism of corrosion and inhibition.[25–32,34] The composition, thickness, and structure of conversion layers were analyzed through top surface and cross-section surface analyses in a point and mapping EDS modes. This article presents the first part of the study, namely on the AA7075-T6 substrate. The following article will present a comparative second part of the study on AA2024-T3.[35]

Table I. Designation of the solutions and samples.

Solution	Abbreviation
0.1 M NaCl	NaCl
0.1 M NaCl + 3 mM $CeCl_3$	NaCl+$CeCl_3$
0.1 M NaCl + 3 mM $Ce(NO_3)_3$	NaCl+$Ce(NO_3)_3$
0.1 M NaCl + 3 mM $Ce(OAc)_3$	NaCl+$Ce(OAc)_3$

a) OAc presents CH_3COO anion.

Experimental

Substrate materials and preparation.—The aluminum alloy AA7075-T6, in 0.6 mm thick sheets distributed by Kaiser Aluminum, USA, was used as substrate. The nominal composition of 7075-T6 alloy given in weight percentage (wt%) is 5.81% Zn, 2.55% Mg, 1.67% Cu, 0.21% Fe, 0.08% Si and the remainder Al. Samples were cut from the sheet. The sample sizes for SEM analysis were 2 cm × 1.5 cm and 4 cm × 2 cm for electrochemical measurements. The samples were water ground up to 4000-grit SiC emery papers (Struers, Denmark), rinsed thoroughly with deionized water, cleaned ultrasonically in ethanol for 10 min and dried with a stream of nitrogen. Samples were then polished on MD-NAP cloth (Struers, Denmark) using a 1 μm diamond paste (DP-Paste 1) and DP-Lubricant Blue (Struers, Denmark), cleaned ultrasonically in ethanol for 10 min, and dried with a stream of nitrogen. The polishing was carried out in ethanol-based lubricant to reduce the possibility of magnesium dissolution during polishing.

Chemicals.—The corrosive medium, 0.1 M NaCl, was prepared with analytical grade NaCl (Carlo Erba 99.5–100.5%). The following cerium(III) salts were used: cerium(III) chloride ($CeCl_3 \times 7H_2O$, 99.9%, Aldrich), cerium(III) nitrate, ($Ce(NO_3)_3 \times 6H_2O$, 99.5%, Fluka), and cerium(III) acetate, ($Ce(CH_3COO)_3 \times nH_2O$, denoted as $Ce(OAc)_3$, 99.9%, Aldrich). The amount of crystal-bound water was calculated from thermogravimetric analysis to give $Ce(CH_3COO)_3 \times 2H_2O$. Cerium salts were dissolved in 0.1 M NaCl solution at 3 mM.[17] Solutions were prepared with deionized water (Milli Q Direct water, resistivity greater than 18.2 MΩ·cm at 25 °C and a total organic carbon (TOC) value below 5 ppb, Millipore, Billerica, MA, USA).

Preparation of samples in NaCl and NaCl + cerium salt solutions.—Polished samples were immersed for 24 h in 0.1 M NaCl solution, with and without added 3 mM Ce-salt. Samples were positioned at the bottom of the 100 ml polyethene vials. Preparation was performed at ambient temperature. After immersion, samples were rinsed with deionized water, dried, and photographed with a digital camera. The designation of the samples is presented in Table I.

The addition of a 3 mM Ce salt changes the pH of the solution: NaCl (pH = 5.5), NaCl+$CeCl_3$ (pH = 5.2), NaCl+$Ce(NO_3)_3$ (pH = 5.3), and NaCl+$Ce(OAc)_3$ (pH = 6.8). The pHs of the solutions were left at its natural values.

The test was carried out in quadruplicate for each substrate and immersion solution: one sample was used for surface analysis, and three were used for electrochemical measurements.

Surface analysis.—SEM images were taken in secondary electron (SE) and backscattered electron (BSE) modes using an FEI Helios Nanolab 650 microscope. EDS spectra were taken using an Oxford Instruments AZtec system with X-max SDD (50 mm^2) detector. The analyzed beam voltage was 5 kV and 15 kV. Single

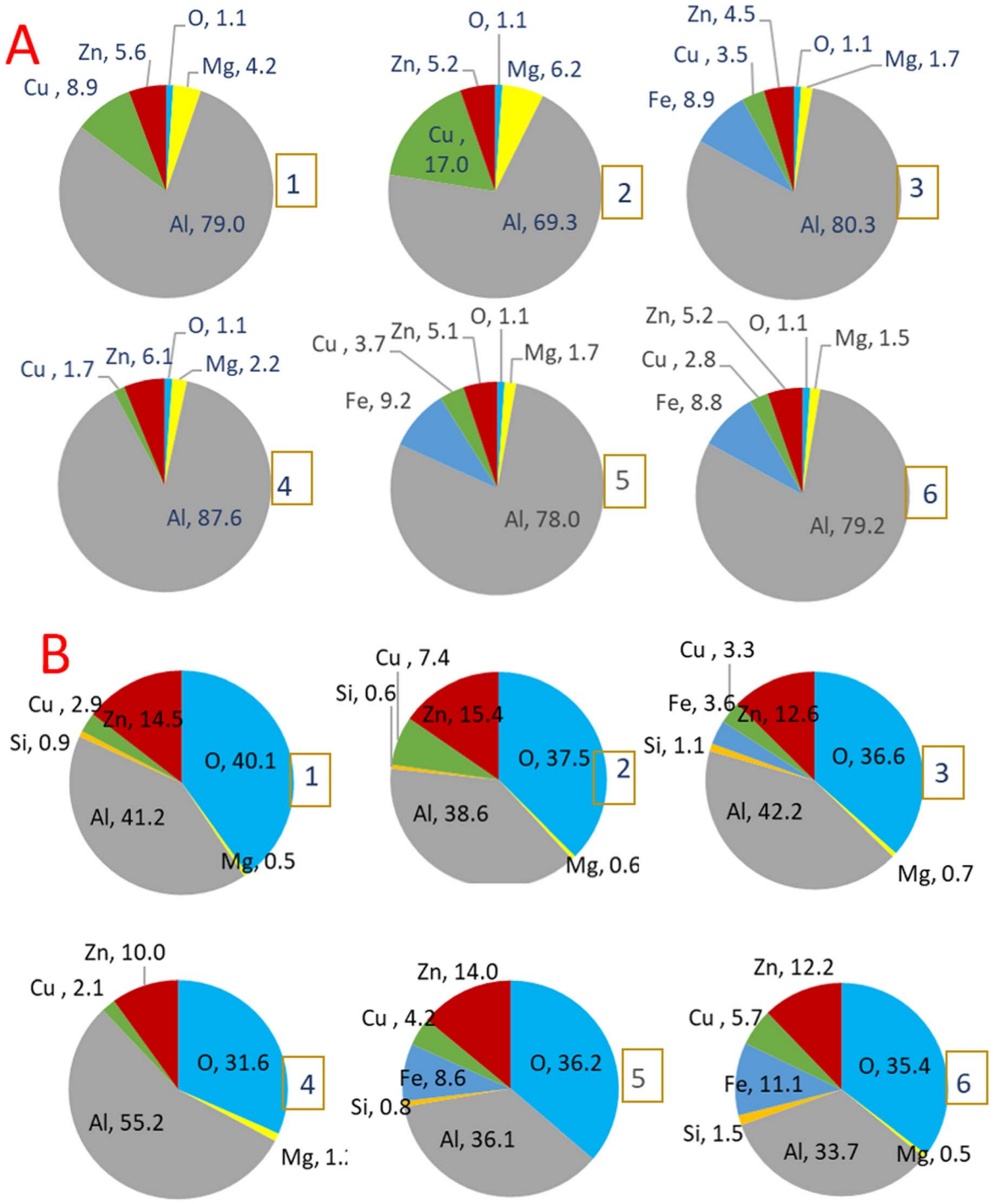

Figure 3. The compositions in wt% measured with EDS are presented as pie graphs. Analyses were made at the sites denoted at SEM images by numerals 1–6 (Fig. 2) before (panel A) and after immersion for 24 h in 0.1 M NaCl (panel B). EDS analysis was carried out at 5 kV.

scattering Monte Carlo simulation program was used to calculate the analysis depth. The simulation is presented in Fig. S1(available online at stacks.iop.org/JES/169/091501/mmedia) for bare and Ce-coated AA7075-T6. The analyzed depth on bare alloy is 1.5 μm at 15 kV, and 280 nm at 5 kV. On the alloy coated with a Ce-conversion layer the analyzed depth is 1.4 μm at 15 kV, and 200 nm at 5 kV. EDS mapping was recorded with 15 kV beam voltage, except for the sample immersed in Ce(III) acetate, where also 5 kV was used. Before analysis, samples were coated with a thin carbon layer to reduce the charging effect.

FIB was used to analyze the cross-section of conversion layers. An FEI Helios Nanolab 650, equipped with EDS, was first used to deposit a 0.2 μm thick Pt protection layer using an electron gun and then a 1 μm thick Pt layer using an ion gun. Then, a relatively large cross-section was made by a rough removal of material with Ga ions (30 kV/21 nA) followed by a rough polishing (30 kV/2.5 nA) and a fine polishing (30 kV/0.4 nA).

The analysis was made at the same site before and after immersion. The area of interest was marked to assist the finding the exact location after exposure to the electrolyte.

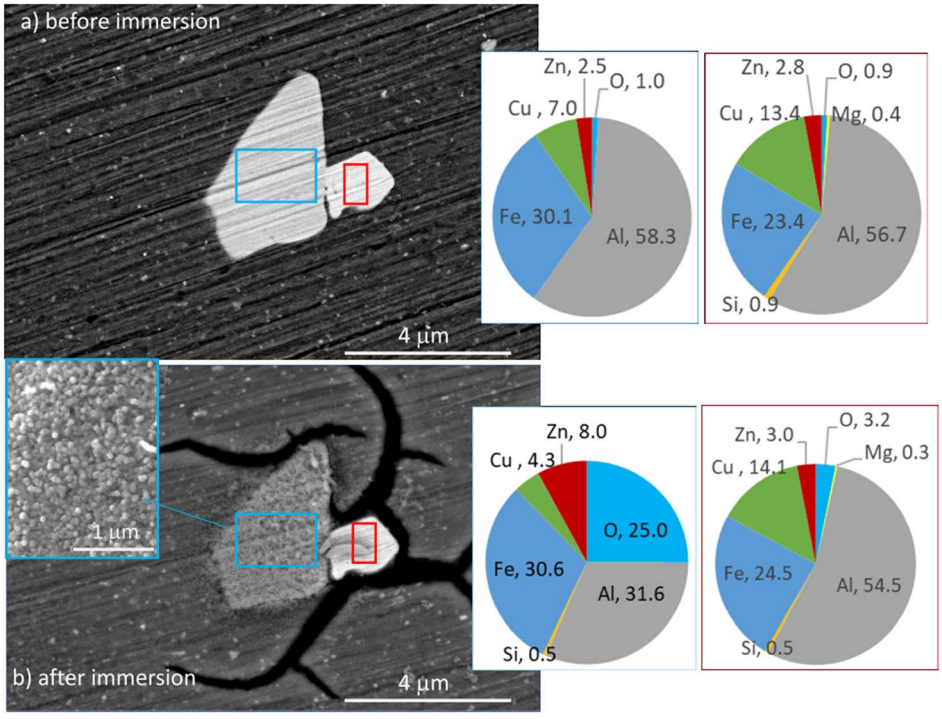

Figure 4. Detail of site 5 in SEM images (Fig. 2) before (a) and after (b) immersion for 24 h in 0.1 M NaCl. The analysis was made at the same site before and after immersion in the electrolyte. The compositions of the sites denoted at SEM images by red and blue rectangles were analyzed by EDS and presented in wt % in the form of pie graphs. Two neighboring Al(Fe-Cu)Si-based IMPs differ in the amount of Cu: the red rectangle denotes the IMP richer in Cu than that denoted by the blue rectangle. SEM images were taken in BSE mode, but the inset in (b) was taken in SE mode; SEM and EDS analyses were performed at 5 kV.

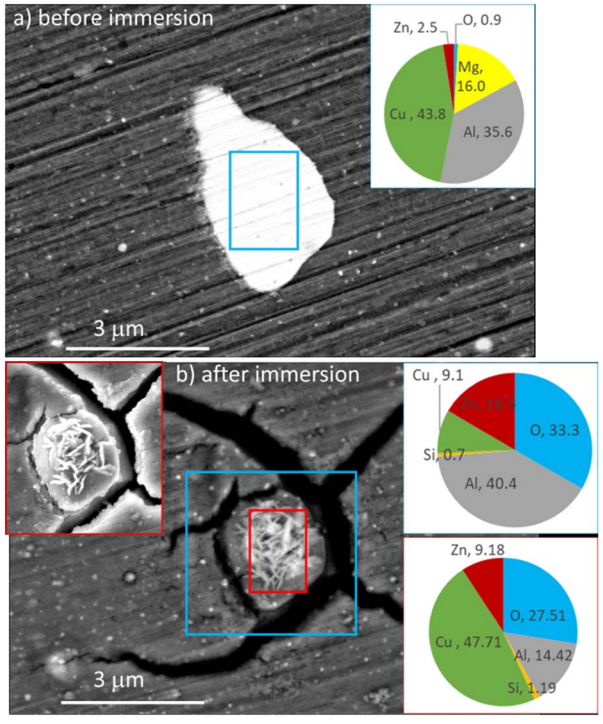

Figure 5. Detail of site 2 in SEM image (Fig. 2) before (a) and after (b) immersion for 24 h in 0.1 M NaCl. The analysis was made at the same site before and after immersion in the electrolyte. The compositions of the sites denoted at SEM images by red and blue rectangles were analyzed by EDS and presented in wt% in the form of pie graphs. S-phase (Al_2CuMg) IMPs contained Al, Cu, and Mg before the immersion but no Mg after immersion. The blue rectangle denotes the area surrounding the Cu-redeposition area. SEM images were taken in BSE mode, but the inset in (b) was taken in SE mode; SEM and EDS analyses were carried out at 5 kV.

The EDS analysis of Ce-conversion layers is not straightforward. When the thickness of the layer is above several hundreds of nanometers, it is possible to use higher voltage in EDS analysis where there is no overlapping between Ce (originating from precipitated layer) and Cu (originating from the substrate) signals. However, the thickness of Ce-conversion layers is under some conditions in the nanometric range, and it is not possible to use the 15 kV voltage in EDS analysis due to the large analysis depth of over 1 micrometer (Fig. S1). Instead, analyses were mainly performed at a low voltage of 5 kV to allow smaller analysis depth concentrated on the top surface. However, it should be taken into account that under these conditions there is an overlapping of Ce Mα and Cu Lα peaks in EDS spectra. Consequently, the error in the determination of composition is relatively high for Ce (higher than the usual 5%). The presence of Ce must be then additionally confirmed by using a somewhat higher voltage (e.g. >8 kV) to detect Ce Lα in addition to Ce Mα overlapping with Cu Lα peaks.

Electrochemical measurements.—Electrochemical measurements were performed in a three-electrode standard corrosion cell (Princeton Applied Research, Flat Cell, model K0235, volume 250 ml) at an ambient temperature of 23 ± 1 °C. Samples pre-immersed for 24 h in 0.1 M NaCl with and without added 3 mM Ce (III) salt were used as working electrodes. For reference, measurements were also performed on the freshly polished, non-immersed substrate. Samples were then embedded in the cell, leaving an area of 0.95 cm^2 exposed to the corroding solution, and served as a working electrode. An $Ag/AgCl_{sat.\ KCl}$ electrode (0.198 V vs saturated hydrogen electrode) was used as a reference electrode. A platinum wire served as a counter electrode. Electrochemical experiments were carried out with an Autolab M204 (Metrohm Autolab, Utrecht, The Netherlands) potentiostat/galvanostat controlled by Nova 2.1 software.

Before the measurements, the samples were allowed to stabilize under open-circuit conditions for 1 h. The stable, quasi-steady state potential is denoted as the open circuit potential (E_{oc}). Following stabilization, anodic and cathodic curves were recorded separately (starting −10 mV vs E_{oc} in the anodic direction and starting + 10 mV vs E_{oc} in the cathodic direction, respectively). For each type of solution, measurements were performed at three different samples, usually at two sites at each sample; therefore, measurements were performed in triplicate or sextuplicate.

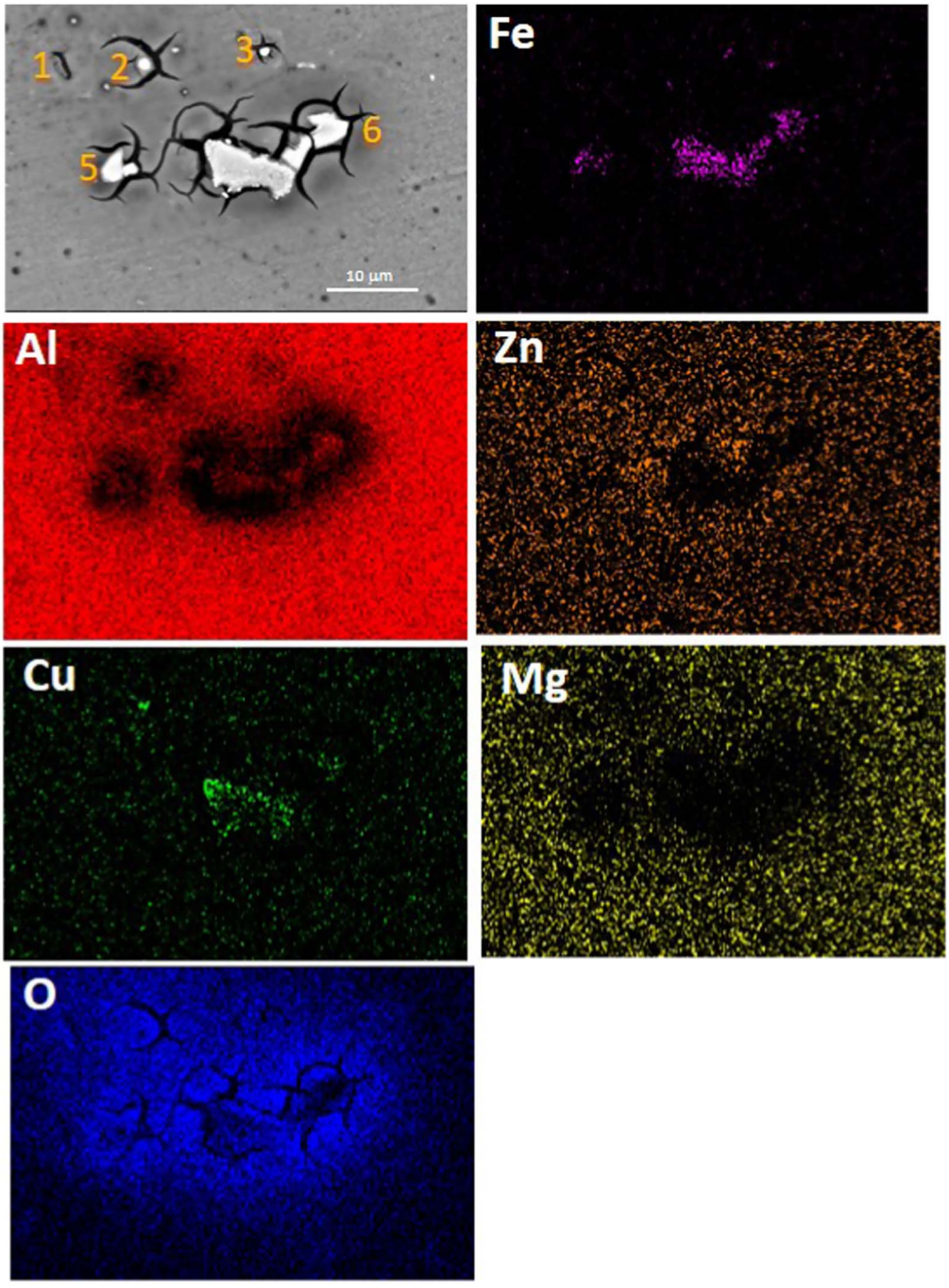

Figure 6. SEM image and EDS elemental mapping of the AA7075-T6 sample after immersion for 24 h in 0.1 M NaCl (Fig. 2, panel B1). EDS mapping (Fe, Al, Zn, Cu, Mg, O) and SEM analyses were carried out at 15 kV. In the SEM image, sites of interest were numbered as in Fig. 2 for easier orientation.

Results and Discussion

General description of AA7075-T6 samples before and after immersion in 0.1 M NaCl without and with added Ce salts.—In this section, we comment on the samples' general description without a detailed description of intermetallic particles. The latter is presented in the next section, individually for each sample. The left panel of Fig. 1 (panel A) presents SEM images recorded in BSE mode on four bare AA7075-T6 samples (images A1−A4) before immersion. The designation of the samples is given in Table I. Samples are characterized by dark alloy matrices and bright IMPs of different sizes and shapes. The samples were then immersed for 24 h in solutions of interest and re-introduced in the electron microscope with the same spot re-analyzed. The right panel of Fig. 1 (panel B) presents SEM images recorded on four samples after immersion in 0.1 NaCl (image B1), 0.1 M NaCl + 3 mM $CeCl_3$ (image B2), 0.1 M NaCl + 3 mM $Ce(NO_3)_3$ (image B3) and 0.1 M NaCl + 3 mM $Ce(OAc)_3$ (image B4). For samples NaCl+$CeCl_3$ and NaCl+$Ce(NO_3)_3$, the spots recorded before the immersion (yellow rectangles in images B2 and B3) were smaller than after immersion. The reason is that we noticed bigger Ce deposits slightly outside the recorded spot and analyzed them subsequently.

After immersion in 0.1 M NaCl for 24 h, the bare sample underwent severe corrosion (image B1). IMPs were covered by

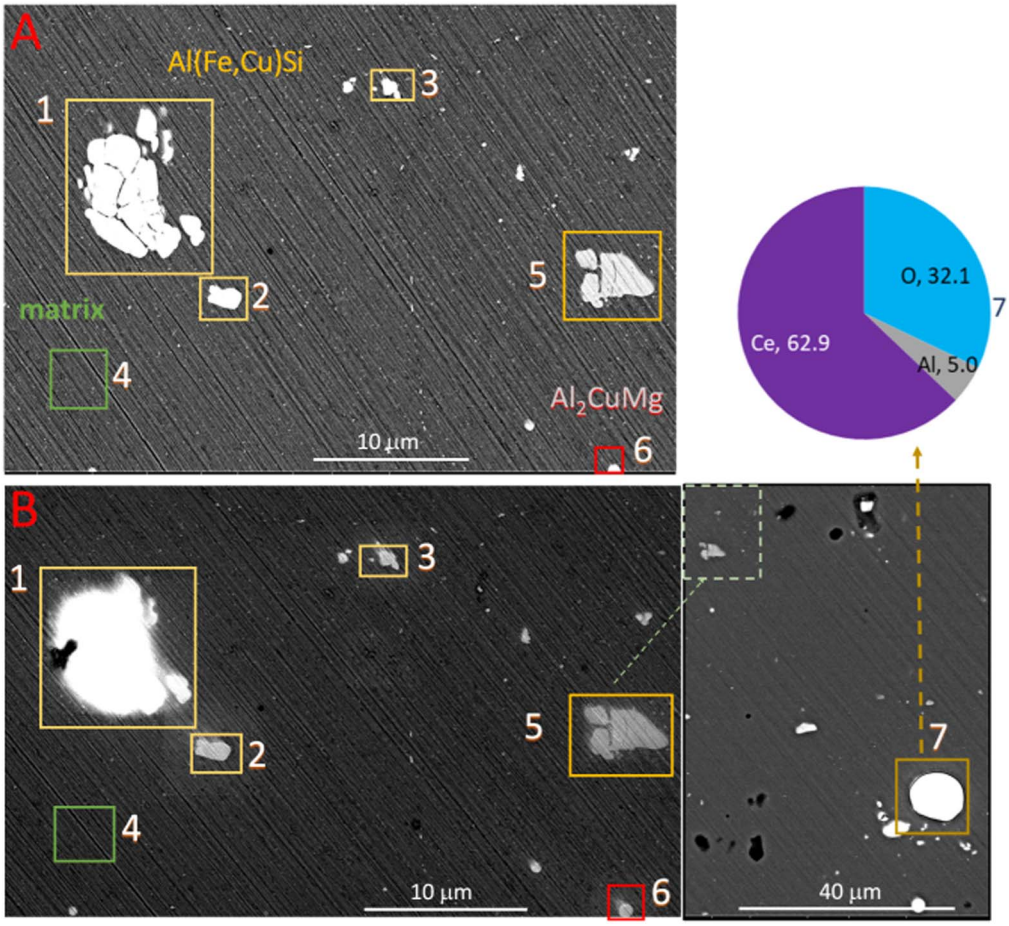

Figure 7. SEM images taken of the AA7075-T6 sample before (A) and after (B) immersion for 24 h in 0.1 M NaCl + 3 mM $CeCl_3$. The analysis was made at the same site before and after immersion in the electrolyte (Figs. 1A2, 1B2). The compositions of the sites denoted at SEM images by numerals 1–6 were analyzed by EDS. EDS composition in wt% is presented as pie graphs in Fig. 8, except for site 7, which is presented herein. The green rectangle denotes the matrix, red rectangles denote Al-Cu-Mg (S-phase) IMP, and yellow rectangles denote Al(Fe-Cu)-based IMPs. SEM images were taken in BSE mode at 5 kV.

corrosion products, which changed the composition of IMPs' surface, as evidenced by the different brightness of the particles. Severe corrosion damage with trenches and micrometer-sized cracks dominate the surface. In contrast, samples immersed in cerium salts did not undergo corrosion, at least not visible at this magnification (images B2–B4). Some IMPs remained virtually intact but covered with bright deposits. The bright color indicates the presence of a heavy element (cerium element has a density of 6.76 g cm^{-3}). At some spots, large deposits were formed which covered the underlying IMP. The first impression is that the samples immersed in Ce chloride and nitrate salts behave similarly, whereas that immersed in Ce acetate differ. In the latter case, IMPs are virtually unchanged, i.e. no visible bright deposit was formed. The surface was covered by large precipitates identified as Ce-acetate (*vide infra*), due to lower solubility in water compared to the other two cerium salts.

In each image, we chose several IMPs or clusters of IMPs to be detailed with SEM/EDS analysis before and after immersion. The following sections present the results obtained for each sample.

AA7075-T6 sample immersed in 0.1 M NaCl.—SEM images of the bare substrate before (upper panel A) and after immersion (lower panel B) in NaCl solution are presented in Fig. 2. Different IMPs of interest are noted: yellow rectangles represent Al(Fe,Cu)Si IMPs and red rectangles represent Al_2CuMg IMP (S-phase). The green rectangle represents spots in the matrix. The composition measured with EDS at numerated rectangular spots is given in Fig. 3 in the form of pie graphs. Each spot is numbered for easier orientation.

In bare AA7075-T6, the main IMPs are constituent particles such as $Al_7Cu_2Fe(Mn)$, $(Al,Cu)_6(Fe,Cu)$, Al_3Fe, of which the former two are most abundant[25] and essential for galvanic activities. We denoted these IMPs by a generic term Al(Fe,Cu)Si for simplicity bearing in mind that is their general composition and that the exact composition is more complicated as described in detail elsewhere.[25,36,37] Al(Fe,Cu)Si IMPs are larger, several micrometers long and irregular in shape. Generally, constituent particles are nobler than the matrix (they have more positive corrosion potential). Other particles include precipitates like Al_2CuMg (S-phase), Al_2Cu (θ phase), $MgZn_2$, Mg_2Si, and dispersoids like Al_3Ti, Al_6Mn.[37] S- and θ phases are usually smaller than constituent particles and may be spherical or elongated. The transition of the S-phase from initially active to nobler relative to the matrix is well described in the literature.[23,24,27,28,34,37] It occurs due to the selective dissolution of Mg and Al and subsequent enrichment in Cu. Latest studies show that also Al(Fe,Cu)Si IMPs are susceptible to dealloying.[25–28]

The AA7075-T6 matrix (Figs. 2 and 3, panel A, spot 4) consists mainly of Al (almost 90 wt%), the rest being Zn, Mg, Cu, and O. Freshly polished sample is immediately covered by a spontaneously formed nanometric thick Al-oxide; the content of the oxygen detected by EDS is only about 1 wt%. After

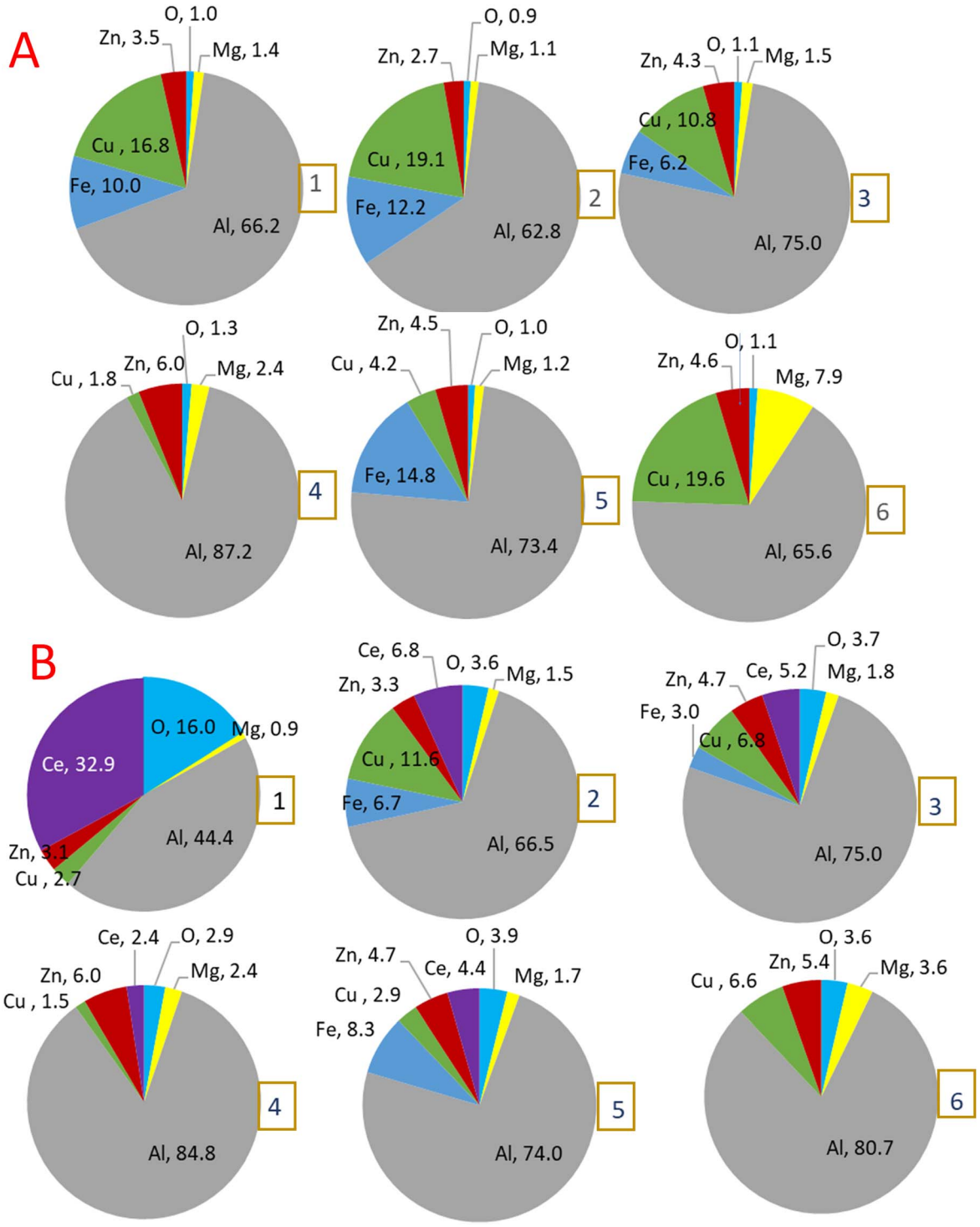

Figure 8. The compositions in wt% measured with EDS are presented as pie graphs. Analyses were made at the sites denoted at SEM images by numerals 1–6 (Fig. 7) before (panel A) and after immersion for 24 h in 0.1 M NaCl + 3 mM $CeCl_3$ (panel B). EDS analysis was carried out at 5 kV.

immersion in NaCl, however, the composition of the matrix changed with oxygen increasing to over 30 wt% (Figs. 2 and 3, panel B, spot 4). During immersion, the Al-hydroxide layer over the matrix was thickening, with no visible corrosion damage observed at this magnification.

A completely different situation was encountered with IMPs (Figs. 2 and 3). Let us start with Al(Fe,Cu)Si. Before immersion (panel A, spots 5 and 6), these large particles, 5–10 μm sized, contained about 10 wt% Fe and 3–4 wt% Cu. Some Zn and Mg were also detected, which belong to the surrounding matrix. After immersion in NaCl, the contours of the IMPs were still visible, but their morphology and composition significantly changed (panel B, spots 5 and 6). Particles were surrounded by wide cracks, over 1 μm thick, which initiated at the IMPs. Cracking was most severe at spot 6, where three IMPs are close to each other (within a 20 μm area). As with the matrix, oxygen content at the IMPs vastly increased relative to the bare sample to over 30 wt%, indicating oxide formation. The content of alloying elements, Fe and Cu, increased as well. The content of Zn increased, whereas Mg was either not detectable or present in well under 1 wt%.

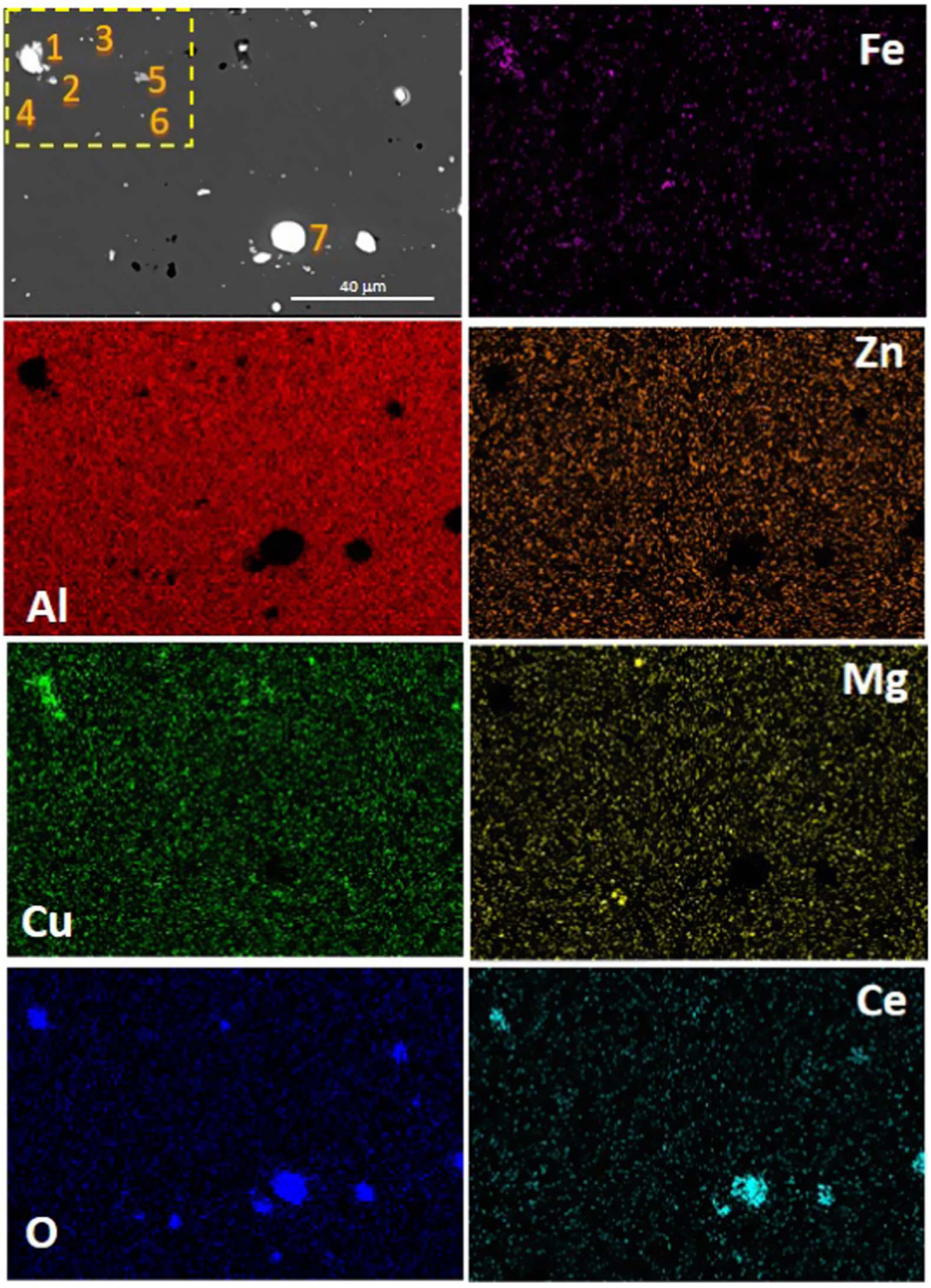

Figure 9. SEM image and EDS elemental mapping of the AA7075-T6 sample after immersion for 24 h in 0.1 M NaCl + 3 mM $CeCl_3$ (Fig. 7, panel B). EDS mapping (Fe, Al, Zn, Cu, Mg, O, Ce) was taken at 15 kV voltage. In the SEM image, sites of interest are numbered as in Fig. 7 for easier orientation. SEM image was taken in BSE mode at 15 kV.

Some analyzed spots consist of several IMPs, i.e. spot 5 consists of two IMPs and spot 6 of at least three IMPs. The surface of some IMPs was covered by a corrosion product, whereas the surface of other IMPs was not covered by this product and remained smooth, i.e., smaller IMP in spot 5 and two IMPs on the right-hand side in spot 6. Large IMP in spot 6 was covered by corrosion product and also sprinkled at the edges by bright spots.

Spot 5 is presented in enlarged images in Fig. 4 before and after immersion to inspect the morphology and composition more closely. More detailed EDS analysis is enabled at a higher magnification than in Fig. 3. Before immersion (Fig. 4a), two IMPs can be identified at this spot: left IMP (blue rectangle) is $\sim$3.5 μm $\times$ 5 μm sized and rich in Fe (30 wt% Fe and 7 wt% Cu) and right IMP (red rectangle) is smaller, $\sim$2 μm $\times$ 1.4 μm sized, and rich in Cu (23 wt% Fe and 13 wt% Cu). After immersion, their composition differed drastically: Fe-rich IMP was wholly covered by Al-hydroxide corrosion product (32 wt % Al and 25 wt% O). Its morphology is in the form of nodules sized around 100 nm (SEM SE image in the inset in Fig. 4b). The Cu content at this IMP decreased to half after immersion. In the BSE image, this product appeared grey, indicating that it is lightweight, i.e. originating from Al. In the SE image (inset), it appears bright.

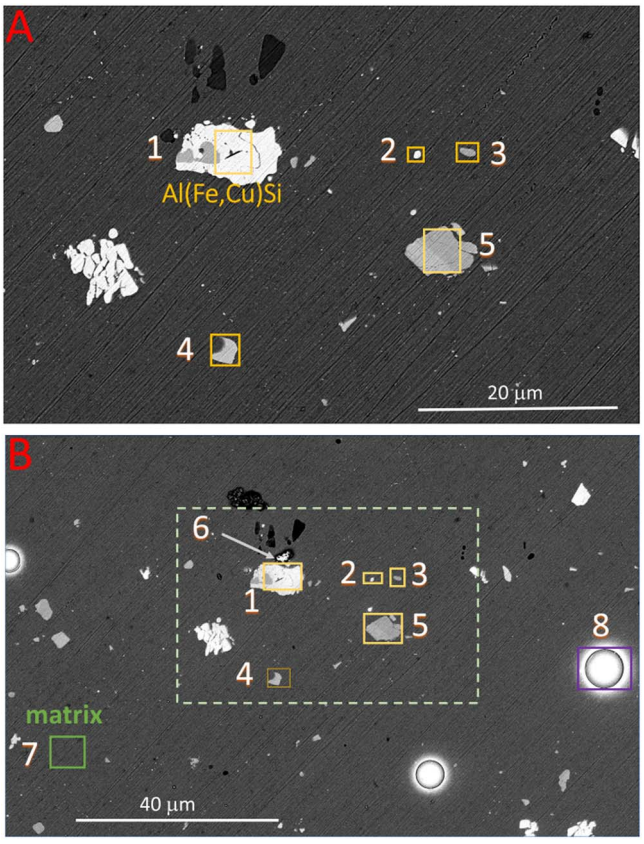

Figure 10. SEM images taken of the AA7075-T6 sample before (A) and after (B) immersion for 24 h in 0.1 M NaCl + 3 mM $Ce(NO_3)_3$. The analysis was made at the same site before and after immersion in the electrolyte (Figs. 1A3, 1B3). The compositions of the sites denoted at SEM images by numerals 1–8 were analyzed by EDS. EDS composition in wt% is presented as pie graphs in Fig. 11. The green rectangle denotes the matrix, and yellow rectangles denote Al(Fe-Cu)-based IMPs. SEM images were taken in BSE mode at 5 kV. Detailed EDS analysis of (a) is given in Fig. S3 and Table SI.

In contrast, smaller Cu-rich IMP (red rectangle) remained smooth and bright in the BSE image and seemed detached from the surface. Its composition did not change much relative to before immersion—it remained rich in Cu, Fe content was similar, and oxygen content increased 3-fold (compared to a 25-fold increase at the blue site. A similar situation is encountered on spot 6 (Fig. 2, panel B), with the largest Al(Fe,Cu)Si particle showing similar nodular morphology of Al-hydroxide product with Cu particles sprinkled around the edges, as shown below. Adjacent particles were not covered by Al-hydroxide corrosion product but were detached from the matrix. These are well visible on EDS mapping (see below Fig. 6). Similar behavior was also observed for the Al(Fe,Cu)Si particle on site 3. It seems that the composition of IMP itself, its size, and neighboring particles determine the type of corrosion attack.[38] When two IMPs of different Cu contents are in contact during prolonged immersion in NaCl solution, the one richer in Cu acts like a stronger cathode (red spot), while the other (blue spot) acts as an anode. Consequently, the latter is subject to the dissolution of lighter elements like Al leading to the formation of aluminate ions, AlO_2^-, and their redeposition in the form of a platelet layer.[39] The selective enrichment of copper at the IMPs surface and its redistribution around the neighboring surface has an essential role in this process,[27,28] as evident in the case of larger IMP (spot 6), which is sprinkled by Cu particles. Also, neighboring particles contribute to cooperative corrosion and act autocatalytically, leading to heavy cracking around IMPs.

Al_2CuMg IMP (sites 1 and 2) show different behavior after immersion than Fe,Cu-containing particles: a smaller particle (site 1) was detached from the matrix, but there were no cracks around it, but a larger particle (site 2) was surrounded by cracks and covered by some product. The latter IMP is detailed in Fig. 5 before and after immersion. Before immersion, this spherical particle was ~4 μm × 2.5 μm sized and consisted of 44 wt% Cu, 16 wt% Mg and 35 wt% Al (Fig. 5a). After immersion, however, the center of the IMP was covered by a corrosion product with platelet-like morphology. Mg was dissolved entirely, and Al was dissolved partially as the composition changed to 48 wt% Cu, 14 wt% Al and 27 wt% O. This result corroborate the selective dissolution of Mg and Al from Al_2CuMg IMP and strong enrichment in Cu.[23,24] Considering the high oxygen content (Fig. 5b), it seems that Cu is in the oxidized form, or oxygen is related to the presence of Al-hydroxide formed around the particle.

EDS mapping was employed to demonstrate the chemical changes on the surface during immersion. It should be noted that the areas presented on panel B (i.e. after immersion) were mapped by the EDS but not the areas on panel A (i.e. before immersion). The reason is that we wanted to avoid the potential effect of electron beam during mapping on the stimulative growth of layer at the same area during subsequent immersion, which would produce an artifact. Therefore, EDS mapping for the non-immersed samples was performed in different areas than panel A and presented in Fig. S2. The EDS mapping of Fig. 2, panel B is presented in Fig. 6. Compared to the mapping of the non-immersed sample (Fig. S2), the most striking difference is the increase in oxygen content and segregation of Cu at the edges of Al(Fe,Cu)Si IMP (site 6). It is also evident that Al_2CuMg IMP (site 2) is depleted in Mg but enriched in Cu after immersion. It should be kept in mind that EDS mapping is illustrative but less sensitive and accurate than point EDS analysis.

AA7075-T6 sample immersed in 0.1 M NaCl with 3 mM $CeCl_3$ added.—SEM images of a selected area on the bare substrate and after immersion for 24 h in 0.1 M NaCl with 3 mM $CeCl_3$ added are presented in Fig. 7. In line with Fig. 2, Al(Fe,Cu)Si IMPs are denoted by yellow rectangles, Al_2CuMg particles by a red rectangle and matrix by green (panel A in Fig. 7). The composition measured with EDS at numerated rectangular spots is given in Fig. 8 in the form of pie graphs. Spots 1, 2, 3, and 5 IMPs contained mostly Fe (6–15 wt%), Cu (4–19 wt%), and Mg (1.1–1.5 wt%) and also differed in size and neighboring particles: spots 1 and 5 are clustered particles (or better say domains), spot 2 is a smaller, individual Fe-Cu rich particle. One Al_2CuMg IMP was noted in this region (spot 6), which is about 1 μm sized spherical particle.

After immersion (panel B in Figs. 7 and 8), an extended area was analyzed compared to panel A, namely site 7, because we noted large bright deposits. The contours of the original site in panel A are noted in the left upper corner by a green rectangle. In contrast to immersion in NaCl (Fig. 2), there was no severe corrosion attack; instead, some IMPs were covered by intensive bright deposits (spots 1 and 7), and others appeared much less bright and virtually unchanged compared to before the immersion. The striking feature is the much lesser oxygen content at the surface than the samples immersed in NaCl solution (except on the most intensively Ce-deposited sites). Contrary to NaCl, where a relatively abundant Al-hydroxide gel is formed, a much thinner layer is formed. This feature was observed for all samples immersed in Ce-containing solutions (*vide infra*). Further, under the conditions used, no layer cracking was noted, leading to the characteristic "dry mud" morphology as observed for different conditions (e.g., the presence of hydrogen peroxide and a higher concentration of cerium salt in immersion bath).[18,40]

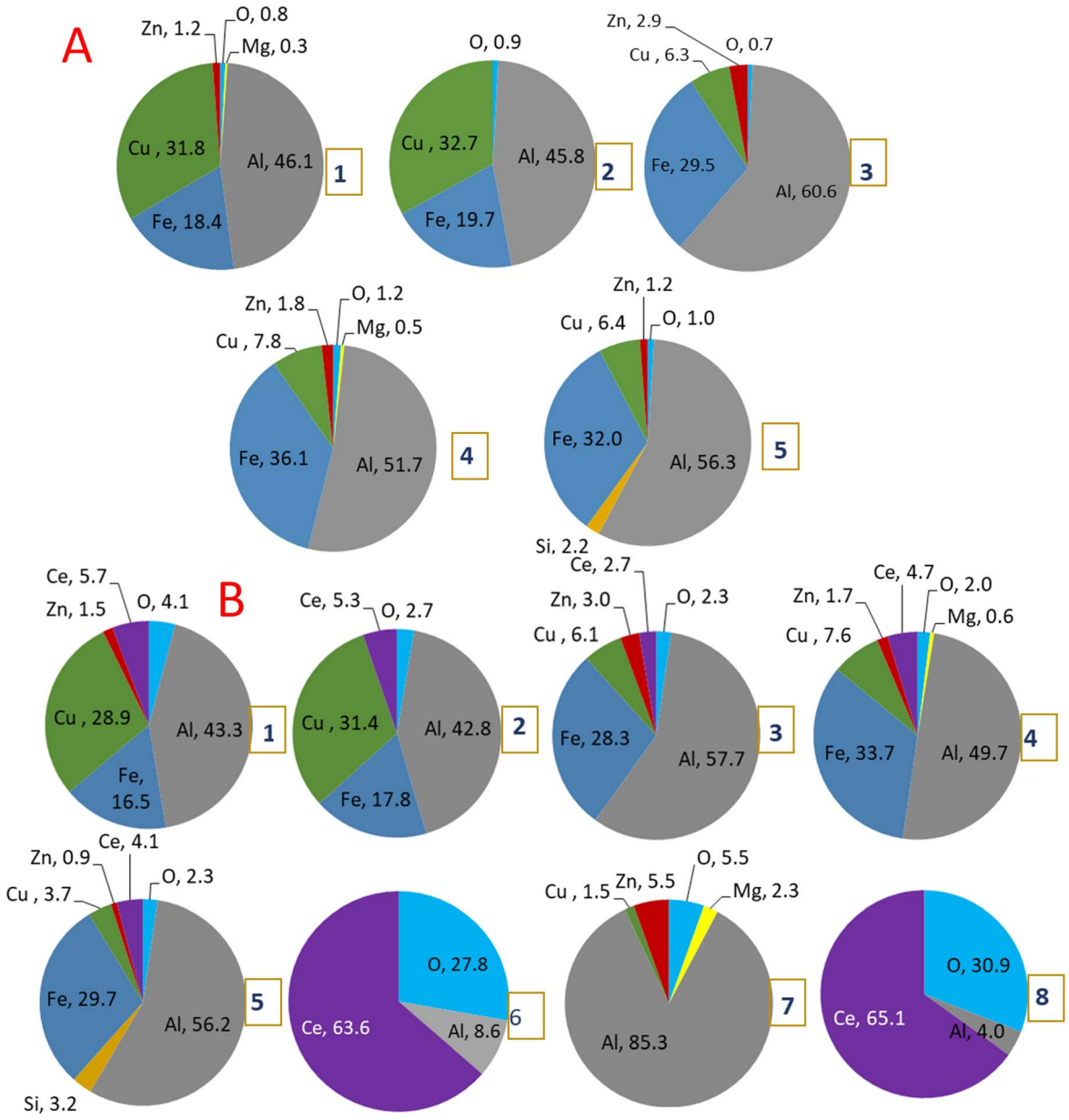

Figure 11. The compositions in wt% measured with EDS are presented as pie graphs. Analyses were made at the sites denoted at SEM images by numerals 1–8 (Fig. 10) before (panel A) and after immersion for 24 h in 0.1 M NaCl + 3 mM $Ce(NO_3)_3$ (panel B). EDS analysis was carried out at 5 kV.

EDS analysis at individual sites (presented in pies graphs in Fig. 8) confirms the formation of Ce oxide at all Fe-Cu-containing sites (1, 2, 3, 5, and 7). The concentration of Ce increased from site 3 (5 wt%) to site 1 (33 wt%) and site 7 (63 wt%). Please consult the *Experimental* section for details concerning the Ce analysis. It seems that the deposition of Ce oxide is not related only to high Cu concentration in IMPs before the immersion (e.g. sites 1 and 2) but also to the size of the particles. The big clustered IMP at site 1 with the total concentration of Cu of 17 wt% was the IMP with the most intensive cathodic sites where the local pH firstly reached the values required for deposition of Ce-hydroxide (pH $>$ 8.5). Smaller sites 2 and 3 were also covered by Ce-hydroxide, but the concentration was several times smaller, similar to in a distant site 5. Sainis et al.[32] showed that the size (lateral spread) of Cu-rich IMP correlated linearly with the amount of deposition in all three directions (x, y, z), while the distance between the neighboring IMPs did not seem to affect the deposition. The most intensive deposition of Ce-hydroxide was noticed on site 7, which we did not initially map before the immersion. However, at this site, we then performed a cross-section analysis (*vide infra*), including a more detailed description of the deposition mechanism.

The network of micro cathodes and anodes spreads all over the surface, and deposition of Ce oxide progressively covers the surface.[9] The deposition of Ce-hydroxide occurs not only at IMPs but also at the matrix. 24 h immersion was a long enough period for the deposition to progressively spread over the whole surface of the sample. It will be shown below that the Ce-rich layer formed over the matrix was less than 100 nm thick. Interesting to note is that at site 6 (Al_2CuMg), no Ce deposition was identified by EDS. However, although Mg content was reduced from 8 wt% (panel A, site 6) to 4 wt% (panel B, site 6), Mg was not wholly dissolved as noticed in uninhibited NaCl solution (Fig. 2, sites 1 and 2). This result indicates that the selective dissolution of Mg from the S-phase is mitigated in the Ce-containing solution. Also, the deposited layer of Ce-oxide may be too thin to be identified by EDS (even at 5 kV).

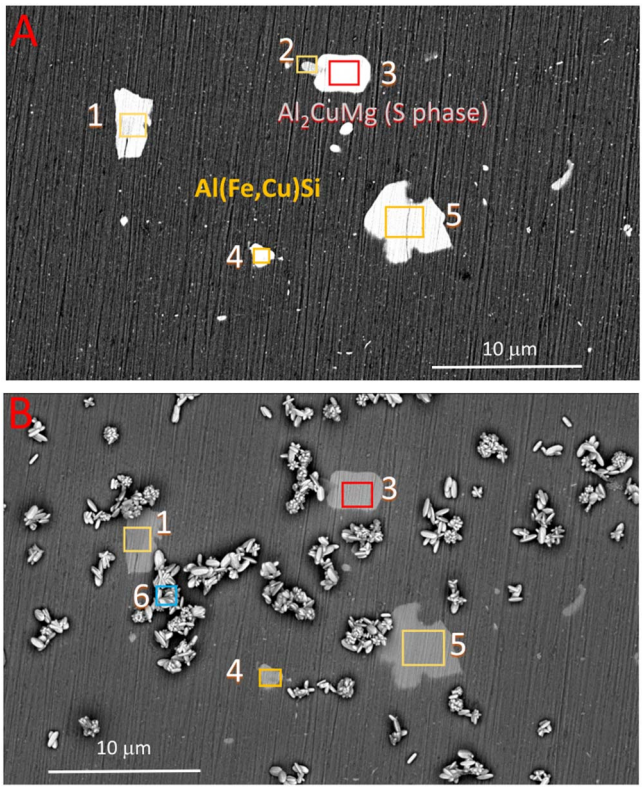

Figure 12. SEM images taken of the AA7075-T6 sample before (A) and after (B) immersion for 24 h in 0.1 M NaCl + 3 mM $Ce(OAc)_3$. The analysis was made at the same site before and after immersion in the electrolyte (Figs. 1A4, 1B4). The compositions of the sites denoted at SEM images by numerals 1–6 were analyzed by EDS. EDS composition in wt% is given as pie graphs in Fig. 13. The red rectangle denotes Al-Cu-Mg (S-phase) IMP, and the yellow rectangles denote Al(Fe-Cu)-based IMPs. SEM images were taken in BSE mode at 5 kV.

EDS mapping depicted in Fig. 9 presents the whole area, including a large Ce deposit (for easier orientation, sites were numbered as in Fig. 7). The areas with large Ce deposits are correlated with significant O content. Since the EDS mapping was taken at 15 kV acceleration voltage, the deposition of Ce hydroxide at the matrix could not be identified (but detected in Fig. 8 at 5 kV). At some sites (spot 5 in the upper corner), Cu content was high and coincided with high Fe content.

AA7075-T6 sample immersed in 0.1 M NaCl with 3 mM $Ce(NO_3)_3$ added.—SEM images of a selected area on the bare substrate and after immersion for 24 h in 0.1 M NaCl with 3 mM $Ce(NO_3)_3$ added are presented in Fig. 10. The composition measured with EDS at numerated rectangular spots is given in Fig. 11 in the form of pie graphs. Only Al(Fe,Cu)Si IMPs denoted by yellow rectangles were analyzed in this sample. It was not easy to find Al_2CuMg particles. Site 1 is a large IMP and consists of several domains with a brighter part containing much more Cu (32 wt% Cu and 19 wt% Fe) than the dark spot in the left corner (7 wt% Cu and 30 wt% Fe) (Fig. S3 and Table SI). Site 5 also consisted of two parts: left, the brighter part with 6 wt% Cu and 32 wt% Fe, and right, darker part with 3 wt% Cu and 32 wt% Fe (Fig. S3 and Table SI). After 24 h immersion (panel B in Figs. 10 and 11), it was striking that no obvious corrosion damage took place. Ce deposition was relatively similar on sites 1–5 showing up to 6 wt% Ce. The most intensive deposition of Ce product was noticed on the small spot near site 1 (site 6), which we did not analyze before immersion. As for the previous sample, we noticed some heavy deposited sites outside the initially analyzed area (site 8); note that the area analyzed before the immersion is denoted by dashed lined. No Ce deposition could be identified at the matrix (site 7) under the experimental EDS conditions.

EDS mapping after immersion is depicted in Fig. S4. The areas with large Ce deposits are correlated with significant O content. The presence of several IMPs with large Cu and Fe content and sites containing Mg were identified (which we did not identify in the initial panel A in Fig. 10). It became clear now that the small site 6 (near site 1) that presented the highest Ce content after immersion was probably Al_2CuMg IMP. Outside the initially analyzed area, several IMPs containing Mg were present.

AA7075-T6 sample immersed in 0.1 M NaCl with 3 mM $Ce(OAc)_3$ added.—SEM images of the selected site on AA7075-T6 before and after immersion for 24 h in 0.1 M NaCl with 3 mM $Ce(OAc)_3$ added are presented in Fig. 12. The composition measured with EDS at numerated rectangular spots is given in Fig. 13 in the form of pie graphs. Five spots were analyzed: sites 1, 2, 4 and 5 are Al(Fe,Cu)Si IMPs, and site 3 is Al_2CuMg (panel A in Figs. 12 and 13). Sites 1, 2 and 5 contained less Cu content than site 4, with over 30 wt% Cu. After 24 h immersion (panel B), the most prominent features are deposits of Ce-acetate over the sample surface (analyzed at site 6). Due to the relatively lower solubility of Ce(III) acetate compared to, for example, Ce(III) chloride and nitrate, prolonged immersion for 24 h led to precipitation at the sample surface in the form of micrometer-clustered globules. However, these globules are not the course of protection of the underlying substrate, which remained non-corroded. EDS point analyses of sites 1 and 5 proved Ce-hydroxide deposition. However, no Ce could be detected at site 4, which remained practically unchanged compared to before the immersion. Most striking is the unchanged composition of S-phase site 3 with fully preserved Mg content. In contrast to Ce(III) chloride and Ce(III) nitrate (Figs. 7 and 10), there were no heavy Ce-containing bright deposits, so the protection mode is different than in the former two solutions.

EDS mapping is presented in Fig. 14. When the analysis was made at 15 kV, the prominent feature was the presence of Ce-based globular precipitates from the solution, which are not the course of protection. When the analysis was made at 5 kV, however, it became evident that Ce-hydroxide deposition occurred over the whole surface, i.e. matrix and IMPs. Namely, a reduction in voltage from 15 to 5 kV decreases the analysis depth from 1.4 μm to 200 nm (Fig. S1).

FIB/SEM/EDS cross-sections of the Ce-deposits and matrix layer.—Cross-section was made at the sample immersed for 24 h in 0.1 M NaCl with 3 mM $CeCl_3$ added. Analysis was performed near spot 7 (depicted by a red rectangle in Fig. 1B2), at two deposits and the matrix. Figure 15a presents the area of interest, where sites 1 and 3 are Ce-product deposits, and site 3 is the matrix. Firstly, site 1 is cross-sectioned by FIB and analyzed at two depths. Figure 15b depicts the cross-section at the first depth, approximately a third of the depth. The dome's interior revealed a matrix containing one large Al(Fe,Cu)Si-based IMP, the interface region between the matrix and the dome. Please note that the carbon and Pt layers were coated for FIB purposes. EDS analysis was performed at various sites in the interior (numbered 1–6), and the results are given in Table II. Site 1 refers to the matrix, and sites 2 and 3 to Al(Fe,Cu) IMPs. In these spots, the content of O was low, around 3 wt%. Site 4 at the interface region reveals a depleted content of Al compared to that at IMPs (for almost 40%), indicating the selective dissolution of Al from IMP and leading to the enrichment in Cu (ratio Al/Cu decreased along the interface). At the same time, the content of O increased 6-fold, and Cl was present. Here Fe is also present in a similar amount as in underlying IMP. An enlarged image of the area around IMP is presented in Fig. 15c. Here we observe the presence of a Cu-rich layer at the surface of IMP. The morphology of this layer is granular.

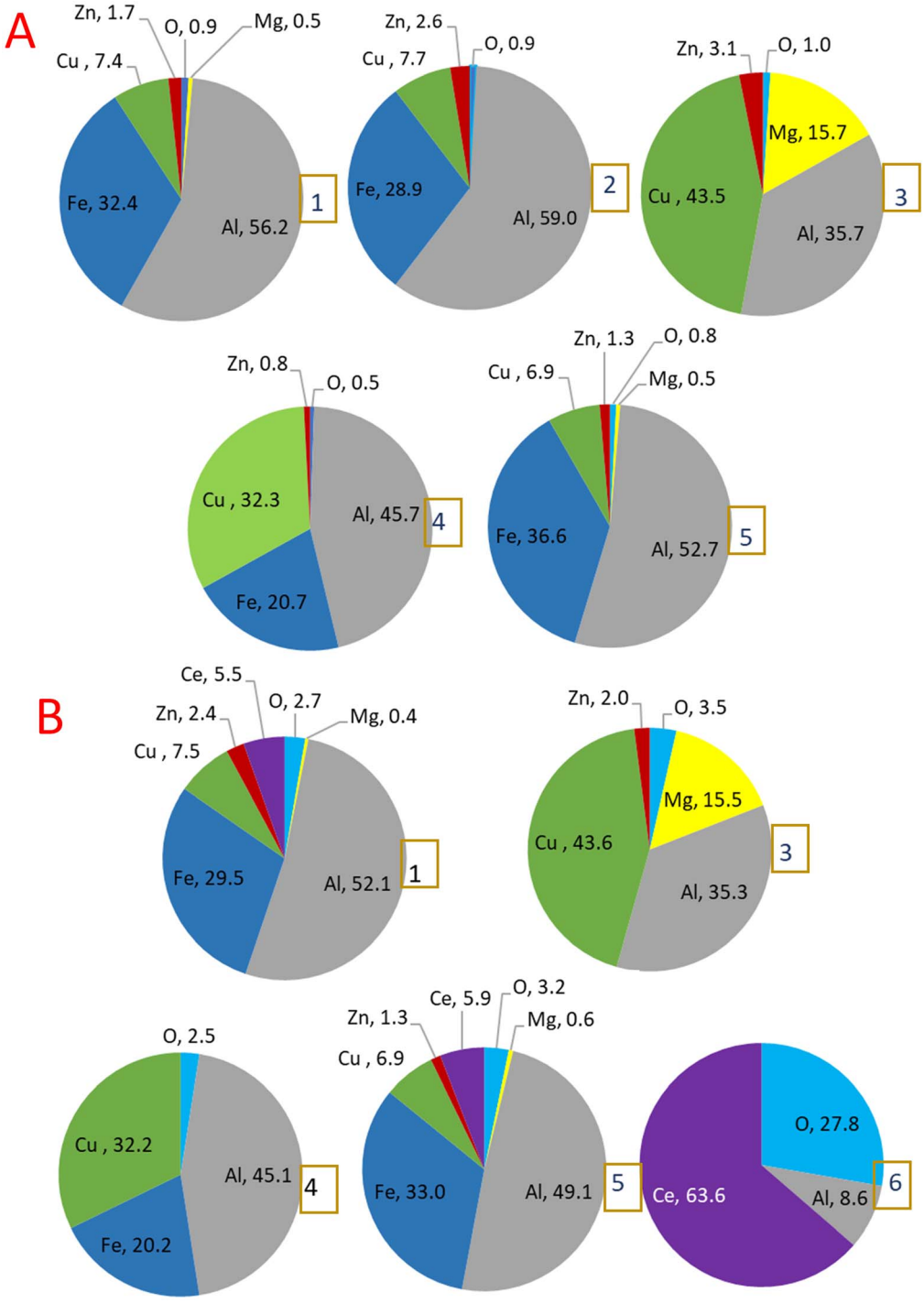

Figure 13. The compositions in wt% measured with EDS are presented as pie graphs. Analyses were made at the sites denoted at SEM images by numerals 1–6 (Fig. 12) before (panel A) and after immersion for 24 h in 0.1 M NaCl + 3 mM $Ce(OAc)_3$ (panel B). EDS analysis was carried out at 5 kV.

There is an intermediate layer between the inner interface enriched in Cu and the dome (site 5); here, Al content was somewhat higher than at the interface, Fe is still present, and O content increased to almost 30 wt% (Table II). A striking feature is a high content of Cl of 7.2 wt%. This intermediate layer still appears dark in the SEM BSE image, indicating that it contains mainly lighter elements. Namely, the dome's interior (spot 6) appeared bright due to the presence of Ce, a heavy element. EDS analysis identified its presence (33 wt% Ce) (Table II). Within the dome, there was no Fe or Cu originating from the substrate; however, the Al content remained relatively high, at almost 30 wt%, i.e. similar to Ce. The presented analysis of the cross-section reveals that within the Ce-containing deposit, there is an inner structure comprising IMP, interface, intermediate layer, and the dome. The enrichment of Cu at the inner interface was reported by Kosari et al.[27,28] using time-resolved TEM and post-mortem SEM/EDS for Cu containing IMPs of AA2024-T3 immersed for 24 h in NaCl with added $Ce(NO_3)_3$. However, several features of the results presented herein are different from the work by Kosari et al.: (i) this is Fe-Cu-containing IMPs of AA7075-T6, which generally exhibit more sluggish kinetics concerning dealloying and Cu enrichment than S- and θ-phases of AA2024; despite that, a sizeable Ce-based deposit was formed

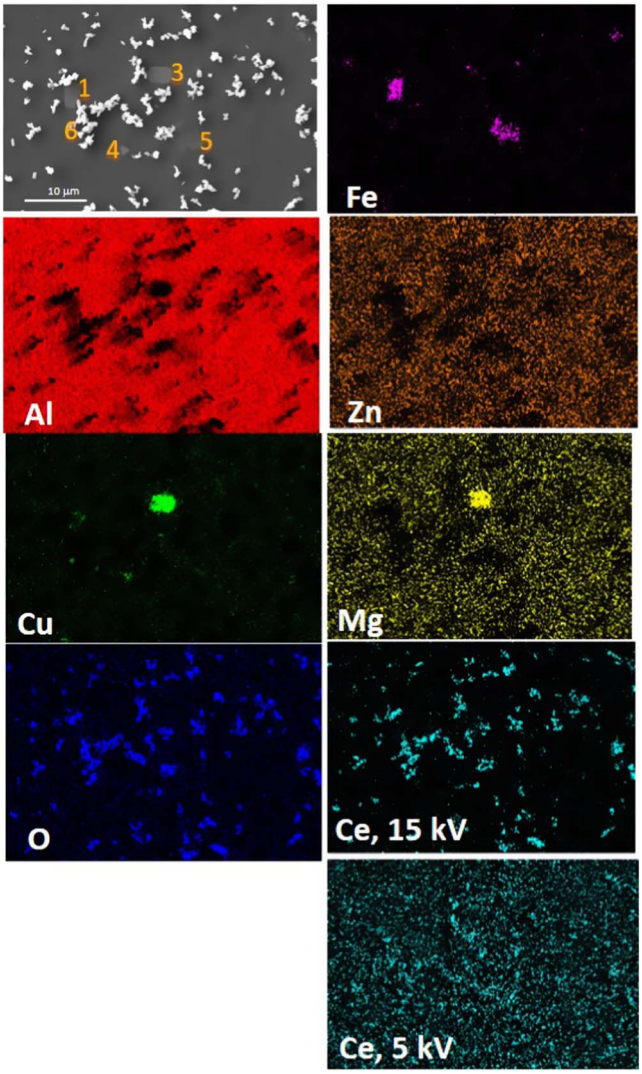

Figure 14. SEM image and EDS elemental mapping of the AA7075-T6 sample after immersion for 24 h in 0.1 M NaCl + 3 mM $Ce(OAc)_3$. (Fig. 12, panel B). EDS mapping (Fe, Al, Zn, Cu, Mg, O, Ce) was taken at 15 kV. Additionally, mapping of Ce was also performed at 5 kV. SEM image was taken in BSE mode at 15 kV.

within 24 h, (ii) chlorine is identified at the interface; in combination with Al depletion, Cu enrichment and O increase it implies that Cl is involved in the initiation of dealloying at the IMPs surface, probably promoting dissolution of Al leaving behind globular Cu interlayer, (iii) there is an intermediate layer between the interface and the dome, where Al, Fe (and Cu) are still present, along with Cl, and (iv) deposit consists of a mixture of Ce- and Al-hydroxides. In our opinion, this behavior can be explained by postulating a "two-way road" process. Namely, Ce-hydroxide deposition was initiated at the Al-depleted site, where the Cu-enriched area became a strong cathode where oxygen reduction occurs. Local alkalinization due to the production of hydroxyl[a] enables the conditions where the precipitation of Ce(III) hydroxide can begin (pH $>$ 8.5). The precipitation of Ce proceeds simultaneously, in a "two-way road" fashion, with Al moving outward and Ce moving inward, leading to the incorporation of Al in the Ce-hydroxide deposit. Kosari et al.[31] observed the formation of $Al(OH)_3$ on the top of Ce-hydroxide deposits and ascribed it to the advanced stage of inhibition where the partial breakdown of Ce-deposits leads to the formation of $Al(OH)_3$ at the ruptured sites. Herein, we observed the incorporation of Al in Ce-deposits since it is present in its interior and not at the top.

Further removal of the deposited material by FIB reveals the composition of the deeper interior within the deposit (Fig. 16). On the right side, two IMPs are now exposed. On the left side, another IMP is present, smaller than the ones at the right hand-site. On the top of all these IMPs, at the interface, Cu-rich granular layer is present. At the edge of the IMP, there was a void that may be related to trenching during the initial phase of corrosion and dealloying, which then progressively ceased as the inhibition process by Ce-deposition progressed. EDS analysis was performed at different spots along the cross-section (Fig. S5, Table SII). The same inner structure of the deposit was confirmed as in the outer depth (Fig. 15b), except Ce was also identified at the intermediate layer (spot 7). This indicates that the center of the deposit, where the initial process started, was now approached (*vide infra*).

Figure 17a shows an enlarged interface image of Al(Fe,Cu)Si IMP covered with a Cu-rich layer (denoted by a red rectangle in Fig. 16). Numbers from the bottom to the top denote the spots where the composition was determined by EDS (Table III) along with the interface depth. Al, Fe, and Cu are detected at the IMP level (spot 1) and its top (spot 2). Two-thirds reduced Al content, i.e. from 55 to 38 wt%, is in line with the selective dissolution of Al. The Fe content remained similar to the IMP. Again, the interface is characterized by higher O content and the appearance of Cl (as observed in Fig. 15b). Right above the interface, in the intermediate layer (spot 3), Ce can now be identified but also Cu, Al, and Fe are still present, although in a lesser amount than at the IMP surface. The ratio Al/Cu decreased from spots 1 to 3, indicating Cu enrichment (Table III). Above this intermediate Ce-Cu-Al-Fe interlayer, Ce further increased, Cu and Fe disappeared, but Al content was still around 12 wt% (spot 4). Chlorine was present in spots 3 and 4. The presented results indicate that Al was dissolving outward from the IMP and reached the most remote spot above the surface. Cerium was not identified in the intermediate layer of the outer area of the dome (Fig. 15b, spot 5) but was identified there at a deeper depth (Fig. S5, spot 7 and Fig. 17a, spot 3). This result concludes that Ce-hydroxide deposition was initiated at the center of the IMP, where the dealloying was the fastest due to the chloride attack. Subsequent enrichment in Cu was the most prominent at this spot, resulting in the transition of the interface to a more cathodic polarity. The latter led to local alkalinization and concomitant deposition of Ce-hydroxide, which then progressed laterally and upwards, forming a large deposit around IMP.

The analysis of the cross-section of the second deposit (spot 2 in Fig. 15a) is presented in Supplementary material (Fig. S6 and Table SIII). It corroborates the structure presented for deposit 1 (Figs. 15 −17).

The schematic presentation of the gradually descending and ascending concentrations of particular elements is presented in Fig. 17b. The interface shows an outward decreasing gradient of Al from IMP to the deposit interior, leaving the interface enriched in Cu. Fe gradient does not change as drastically as Cu; it is similar at the IMP and interface and vanishes towards the deposit interior. Cerium shows an opposite gradient; its concentration rises rapidly from the Cu-rich interface, and it becomes mixed with Al, Cu, and Fe in the adjacent intermediate layer. Oxygen content increased from the interface toward the deposit's interior. Chlorine content is maximized at the interface and reduced within the dome, indicating that Cl is associated with dealloying.

Finally, Ce-hydroxide deposition at the matrix was considered. Figure 18 presents the cross-section of the layer formed at the matrix, away from IMP. Above the matrix, a layer of Al-hydroxide, a few nanometer-thick, was formed. This layer is overtopped with a Ce-hydroxide layer, about 80 nm thick. EDS analysis was performed at enumerated spots, and the results are given in Table IV. Spot 1 refers to the matrix, and spot 2 to the Ce-hydroxide layer. It is difficult to judge whether Al identified in spot 2 originates from the underlying layer, or the Ce-hydroxide layer incorporates Al (as in

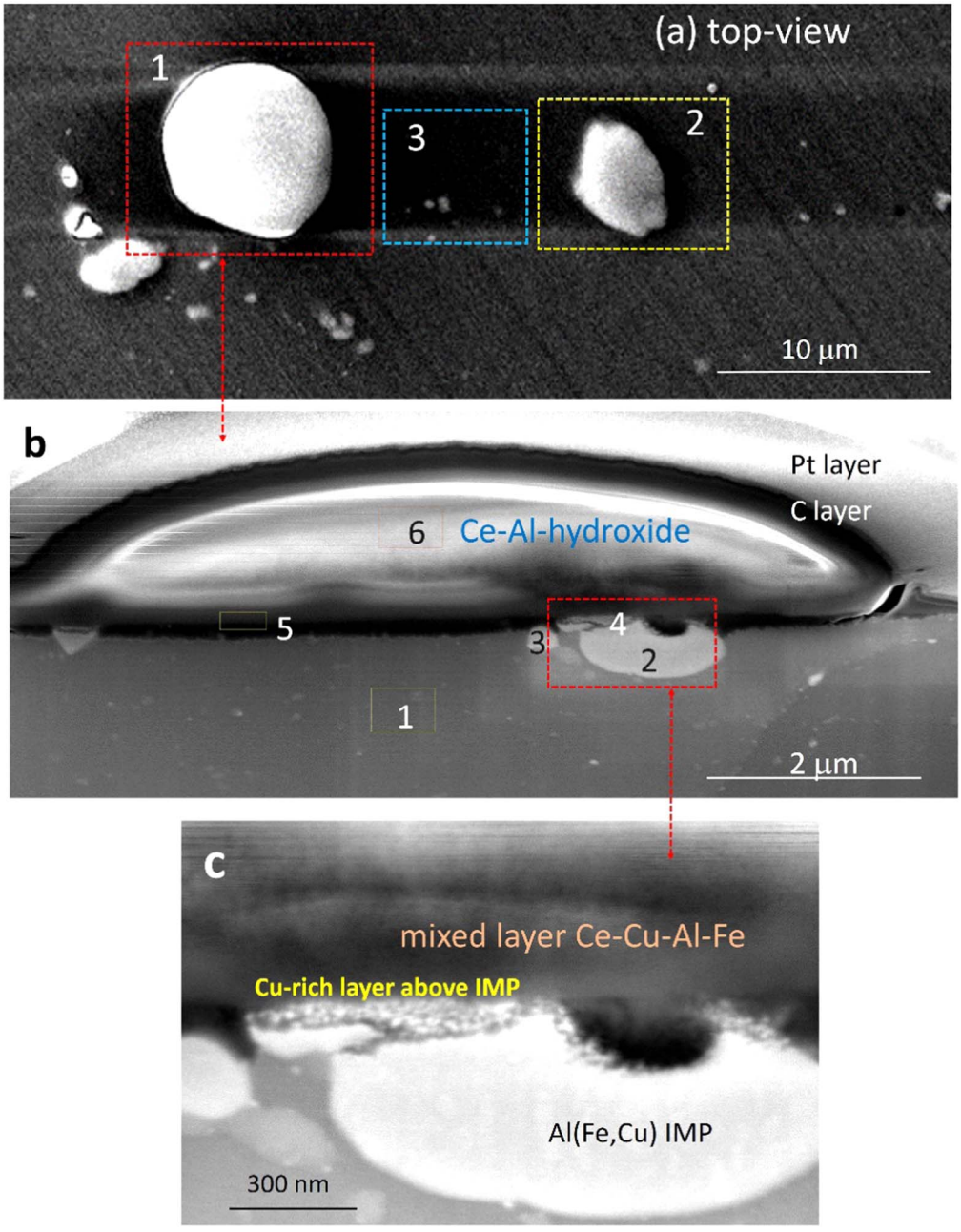

Figure 15. (a) SEM (BSE mode) top-view of the site at which the FIB/SEM/EDS analysis was made of the AA7075-T6 sample after immersion for 24 h in 0.1 M NaCl + 3 mM $CeCl_3$ (denoted by the red rectangle in Fig. 1B2): Ce-hydroxide deposits (domes) 1 and 2 and the matrix site 3. Cross-section images and composition of site 1 are given in (b) and (c). (b) After removal of the third deposited dome by FIB, the inside structure of the dome is revealed to show a Ce-containing deposit over Al(Fe-Cu)-based IMP. The numerals denote the sites where EDS analysis was performed. The resulting compositions are given in Table II. The red rectangle refers to the interface detail depicted in (c). (c) Detail shows the IMP covered with a Cu-rich surface layer overtopped with a mixed layer of Ce-Cu-Al-Fe-hydroxide. This layer also contains some chlorine. SEM and EDS analyses were carried out at 5 kV. SEM/EDS cross-section analysis of spots 2 and 3 presented in top-view (a) is given in Fig. S6 and Table SIII in Supplementary material and Fig. 18, respectively.

the case of deposit). However, no Cl was present, which indicates that at the matrix, a different mechanism was operative as described above for the formation of large deposits. It was proposed that the precipitating Ce-hydroxide progressively exchanges with underlying Al-hydroxide.[1,2] Since there is no prominent cathode at the matrix to induce a burst of hydroxyl ions required for the precipitation of Ce-hydroxide, the deposition progresses slowly through a network of micro-anodes and micro-cathodes at the matrix. The thickness of the precipitated layer at the matrix (less than 100 nm) is approximately 50–100-times smaller compared to that above electrochemically more active IMPs (0.5–1.5 μm).

Electrochemical properties of AA7075-T6 immersed for 24 h in 0.1 M NaCl without and with Ce(III) salts added.—After 24 h in 0.1 M NaCl with and without added 3 mM Ce(III) salts, AA7075-T6 samples were subject to electrochemical measurements in 0.1 M sodium chloride solution. A freshly polished sample (not pre-immersed) was also measured for reference. Before the measurements, the samples were allowed to stabilize under open-circuit conditions for 1 h. The curves showing the open circuit potential (E_{oc}) as a function of time (t) are presented in Fig. 19a. The shape of the E_{oc} vs t curves differed among the samples: upon immersion, the freshly polished sample showed the most negative E_{oc}, around

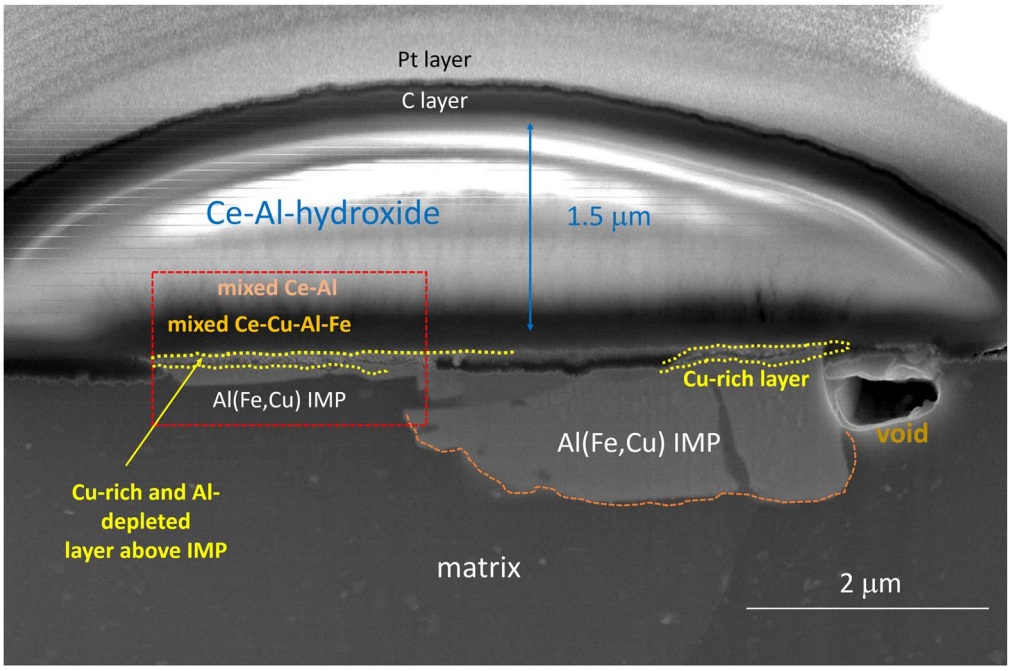

Figure 16. Further removal of material by FIB of the deposit given in Fig. 15 reveals two Al(Fe-Cu)-based IMPs within the matrix and Ce-containing hydroxide deposition over a Cu-rich surface. The red rectangle denotes the interface detail depicted in Fig. 17a, showing a Cu-rich/Al-depleted layer above IMP, mixed Ce-Cu-Al-Fe- overtopped with a thick layer of Ce-Al-hydroxide. This layer also contains some chlorine. On the right-hand side of the IMP, a void was observed, probably related to the initial trenching process. SEM and EDS analyses were carried out at 5 kV. EDS analysis performed at the presented site is given in Fig. S5 and Table SII in the Supplementary material.

Table II. Results of the EDS analysis performed on the numbered spots in SEM image (red rectangle) of AA7075-T6 immersed for 24 h in 0.1 M NaCl + 3 mM $CeCl_3$ (Fig. 15b). The composition refers to the interface between Al(Fe,Cu) IMP and Ce-containing deposit.

Numbered spots	Composition (wt%)							
	O	Mg	Al	Cl	Fe	Cu	Zn	Ce
1	3.0	2.5	88.0	—	—	1.5	5.0	—
2	3.3	—	50.9	—	16.0	29.8	—	—
3	4.5	—	51.5	—	16.2	27.8	—	—
4	19.7	—	34.1	5.4	17.5	23.3	—	—
5	27.9	1.4	48.1	7.2	11.9	—	3.5	—
6	28.0	—	29.7	9.3	—	—	—	33.0

Table III. Results of the EDS analysis performed on the numbered spots in SEM image (yellow rectangle, from bottom to top) of AA7075-T6 immersed for 24 h in 0.1 M NaCl + 3 mM $CeCl_3$ (Fig. 17a). The composition refers to the interface between Al(Fe,Cu) IMP and Ce-Al-hydroxide with a Cu-rich/Al-depleted layer and mixed Ce-Cu-Al-Fe layer. Interface and mixed layer contain O and Cl.

Numbered spots	Composition (wt%)					
	O	Al	Cl	Fe	Cu	Ce
4	26.7	12.3	5.1	—	—	55.9
3	25.9	13.8	4.3	5.3	11.0	39.7
2	20.1	40.1	8.5	14.8	16.5	—
1	4.2	55.4	—	14.5	25.9	—

Table IV. Results of the EDS analysis performed on the numbered spots in SEM image of AA7075-T6 immersed for 24 h in 0.1 M NaCl + 3 mM $CeCl_3$ (Fig. 18). The composition refers to the matrix surface.

Numbered spots	Composition (wt%)						
	O	Mg	Al	Cl	Cu	Zn	Ce
1	3.4	2.2	88.9	—	1.3	4.2	—
2	17.8	4.2	42.4	—	—	—	35.6
3	21.4	—	24.4	7.1	—	—	47.1

−0.8 V, which quickly shifted to a positive direction and, after about 500 s, attained the relatively constant value of −0.63 V. Negative shift in E_{oc} upon immersion is related to the presence of Mg and Zn in the alloy, which both present more negative standard electrode potentials than aluminum.[b] In contrast, after 24 h immersion in 0.1 M NaCl, E_{oc} was at −0.59 V over 200 mV more positive than for

[b]The samples were polished in the absence of water to minimize the dissolution of Mg (and Zn) during surface preparation. Due to the high content of Zn and Mg in the alloy, AA7075-T6 has a rather negative corrosion potential upon immersion in NaCl; once the Al-oxide is formed, the potential retains positive value.

Table V. Cathodic current density at −0.75 V and anodic current density at −0.60 V for curves presented in Fig. 19.

AA7075-T6 samples	Current density in cathodic branch at −0.75 V (A cm^{-2})	Current density in anodic branch at −0.60 V (A cm^{-2})
Freshly polished	3.87×10^{-6}	8.50×10^{-5}
Pre-immersed for 24 h in 0.1 M NaCl	4.02×10^{-6}	8.68×10^{-8}
Pre-immersed for 24 h in 0.1 M NaCl + 3 mM $CeCl_3$	2.56×10^{-6}	5.68×10^{-5}
Pre-immersed for 24 h in 0.1 M NaCl + 3 mM $Ce(NO_3)_3$	2.89×10^{-7}	1.65×10^{-6}
Pre-immersed for 24 h in 0.1 M NaCl + 3 mM $Ce(OAc)_3$	9.69×10^{-8}	7.27×10^{-7}

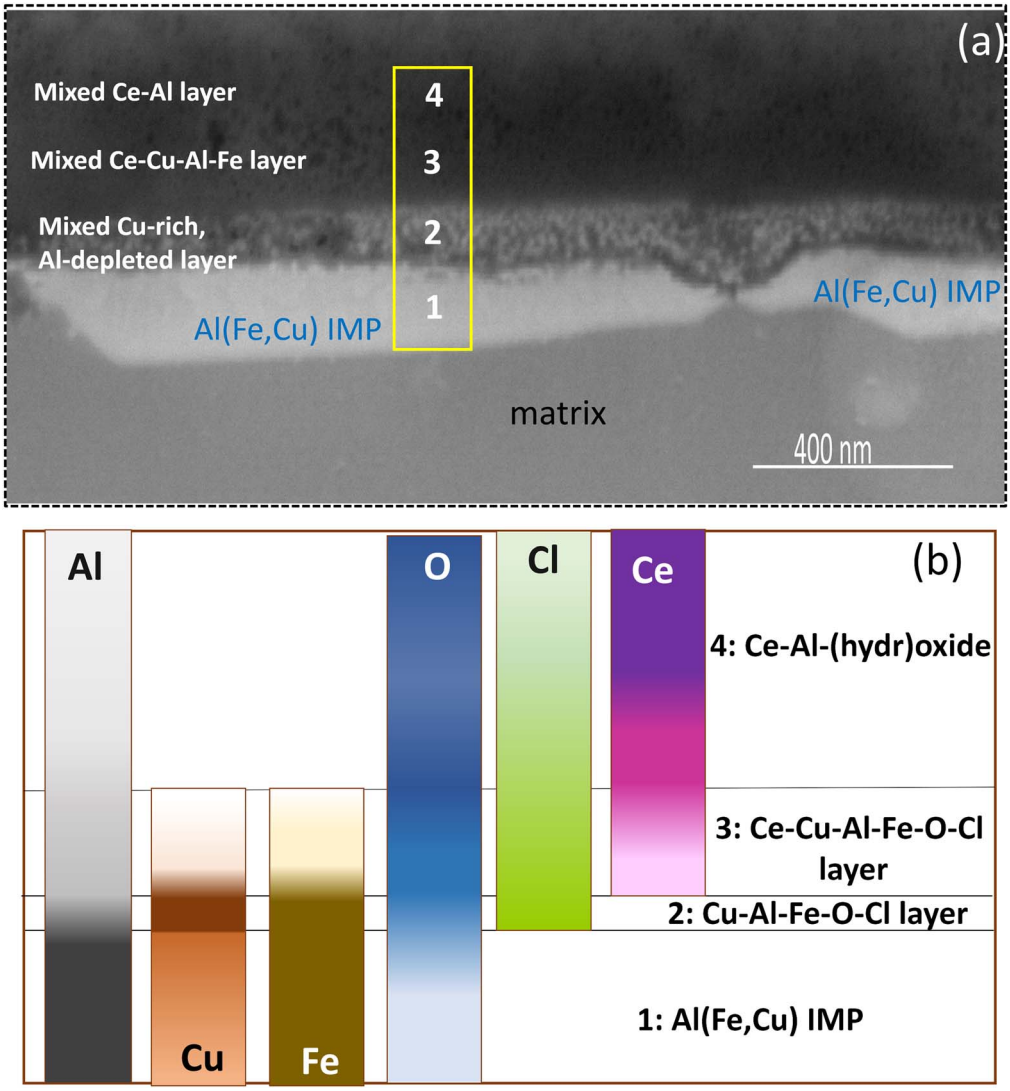

Figure 17. (a) Enlarged image of the interface (denoted by the red rectangle in Fig. 16) between Al(Fe,Cu) IMP and Ce-Al-hydroxide with a Cu-rich/Al-depleted layer, mixed Ce-Cu-Al-Fe layer, and mixed Ce-Al layer (from bottom to the top). Numbers within the yellow rectangle refer to the spots where the EDS analysis was made. The resulting compositions are given in Table III: Spot 1: Al(Fe,Cu) IMP. Layer 2: mixed Cu-rich/Al-depleted interface layer which contains Fe, some O, and also Cl. Layer 3: mixed Ce-Cu-Al-Fe layer with smaller contents of Cu and Fe than in Layer 2 and larger content of O. Layer 4: mixed Ce-Al-hydroxide layer, which also contains some Cl. (b) Schematic presentation of the distribution of Al, Cu, Fe, Ce, O, and Cl at the interface due to dealloying of Al and enrichment of Cu at the interface and simultaneous deposition of Ce-hydroxide on the top leading to the formation of the mixed Ce-Cu-Al-Fe and Ce-Al layers. The interface is overtopped with a thick layer of Ce-Al-hydroxide which contains a small content of Cl. SEM and EDS analyses were carried out at 5 kV.

freshly polished sample reflecting the formation of the oxide layer during immersion which shifted to potential to the positive direction. After 1 h, E_{oc} shifted only 10 mV, i.e., to −0.60 V.

The NaCl+$CeCl_3$ and NaCl+$Ce(NO_3)_3$ samples exhibited similar curves as the NaCl sample but shifted to the negative direction for approximately 50–60 mV reaching −0.66 V at the end of the stabilization period. The most negative E_{oc} was presented by the NaCl+$Ce(OAc)_3$ sample, stabilized at −0.70 V.

The E_{oc} vs t curves reflect different actions of Ce-salts. Compared to chloride and nitrate, Ce(III) acetate can quickly and most efficiently shift E_{oc} in the negative direction. It seems that the fast inhibition kinetics of the formation of the Ce conversion layer in the presence of acetate anions contribute to its action as a stronger cathodic inhibitor compared to the other two anions. This is also reflected in the potentiodynamic polarization curves.

Separately measured anodic and cathodic polarization curves are presented in Figs. S7 and S8 and representative chosen curves are given in Figs. 19b and 19c. Generally, the cathodic reaction is related to the oxygen reduction reaction that proceeds primarily at the IMPs, as described previously.[25] At potentials above E_{corr} (referred to as the stableE_{oc} after the stabilization period of 1 h), dissolution in the anodic region proceeds fast due to localized corrosion.[25] The freshly polished sample exhibited more positive E_{corr} than the sample immersed for 24 h in 0.1 M NaCl (Fig. 19). This indicated that the oxide layer formed on the AA7075-T6 matrix acts protectively despite corrosion damage at IMPs (Fig. 2). Two potentials were selected in cathodic (−0.75 V) and anodic (−0.60 V) branches to compare the current densities of different samples (Table V). At potentials more cathodic than E_{corr} (i.e., −0.75 V), the sample pre-immersed in NaCl reached similar cathodic currents as the freshly polished sample. However, in the anodic region, it exhibited three orders of magnitude smaller current densities than the freshly polished sample.

The NaCl+$CeCl_3$ sample exhibited a very similar E_{corr} to the non-immersed sample, but the cathodic currents were twice smaller. In the anodic range, the curve was similar to the non-immersed sample, indicating the immersion in NaCl containing $CeCl_3$ did not inhibit the anodic reaction (Table V).

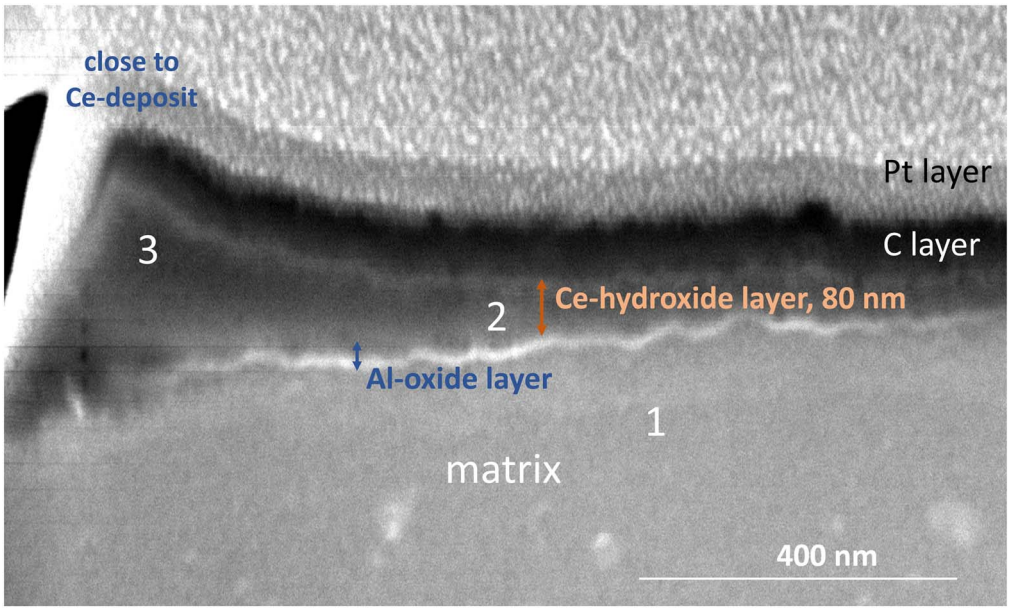

Figure 18. FIB/SEM/EDS analysis of the matrix of the AA7075-T6 sample after immersion for 24 h in 0.1 M NaCl + 3 mM $CeCl_3$ (site 3 denoted in red rectangle in Fig. 1B2 and Fig. 15a). Cross-section made at the matrix showing a thin Al-oxide layer over alloy matrix, few nanometres thick, and top Ce-Al-hydroxide layer, cca. 80 nm thick. EDS analysis was made at the numbered spots, and the resulting compositions are given in Table IV. SEM and EDS analyses were carried out at 5 kV.

The effect of pre-immersion of AA7075-T6 in NaCl with added $Ce(NO_3)_3$ is larger than with added $CeCl_3$ (Fig. 19). Cathodic curve was shifted more negative to −0.68 V and current densities were further reduced to over one order of magnitude. In the anodic range, the change was evident by a small pseudo passive region at −0.61 V was established, extending just 10–20 mV. At more positive potentials, the current increased, indicating localized corrosion. Still, the current density at −0.60 V was two orders of magnitude smaller than for the sample pre-immersed in NaCl (Table V).

The most improved corrosion protection was observed for the samples pre-immersed in NaCl+$Ce(OAc)_3$. In the cathodic range, the currents were almost two orders of magnitude smaller than for the NaCl sample. E_{corr} was shifted in the negative direction to −0.72 V, reflecting the decreased kinetics of oxygen reduction reaction. In the anodic range, a passive plateau was established at −0.68 V, extending for cca. 100 mV.

The reduction of both cathodic and anodic activities depended on the type of Ce salt used. On the cathodic branch, the reduction in the current density compared to the layer formed in non-inhibited NaCl follows the order: chloride < nitrate < acetate, with corrosion potential progressively shifting more negative. In the anodic branch, the same order of current reduction was operative. Layers formed in nitrate and, especially, acetate solutions even exhibited a passive range. Therefore, although the thickness of the Ce-conversion layer was the smallest when formed from Ce(III) acetate salt, it assured the highest degree of protection of the underlying 7075-T6 substrate. Micrometer-thick deposits formed from chloride and nitrate salts were less protective than the thin layer formed in acetate solution. This seems contradictory, but the results indicate that the critical factor for achieving good protection of Ce-conversion layers is to mitigate the selective dealloying of the IMP, which was best achieved in an acetate-containing solution.

Conclusions

We studied the cerium conversion layers formed during 24 h immersion of AA7075-T6 in 0.1 M NaCl with added three types of 3 mM Ce(III) salt: chloride, nitrate, and acetate. Using site-specific FIB/SEM/EDS analysis before and after immersion, we could identify the morphological and composition changes on the surface induced by the conversion of the salt to form insoluble cerium hydroxide. In the NaCl solution, all IMPs were susceptible to dealloying. In the Al_2CuMg S-phase, dealloying of Mg and Al led to Cu enrichment and intensive dissolution of the surrounding matrix leading to heavy cracking around IMP. In the constituents particles Al(Fe,Cu)Si, dealloying of Al also led to the enrichment in Cu, thus contributing to a stronger cathodic character. IMPs in contact with a stronger cathode were subject to intense dissolution, forming an Al hydroxide platelet layer. Dealloying of intermetallic particles eventually resulted in a heavy dissolution of the surrounding matrix with cracking and trenching. The content of oxygen increased considerably.

Adding Ce(III) chloride and nitrate to NaCl considerably reduced the corrosion attack on AA7075-T6. Cracking and trenching were absent. Instead, the surfaces were covered by Ce-rich deposits, progressively forming at the surface. Deposition of Ce-rich layer initiated at the large Cu-containing Al(Fe,Cu)Si IMPs. The deposition proceeded laterally across the surface, from IMP to IMP, depending on the intensity of dealloying and consequent electrochemical activity, making some IMPs more sluggish than others in the process of Ce-precipitation. The deposition also proceeded at the matrix.

Cross-section analysis of large deposits brought new details of the operative mechanism of Ce deposition. Dealloying of Al from Al(Fe,Cu)Si constituent particle leaves behind the layer strongly enriched in Cu in the form of globular remnants. Therefore, this mechanism is not operative only for S-phase but also for Fe,Cu-containing IMPs. Another novel finding is the presence of chlorine at the inner interface, indicating that chloride ions promote the selective dissolution of Al. The surface of IMP left behind enriched in Cu becomes a strong cathode where oxygen reduction takes place, leading to local alkalization required for Ce-hydroxide precipitation. At large IMPs, the process can be so intense that the bursting electrochemical activity results in the precipitation of micrometer-sized deposits. The formation of the conversion layer is a dynamic process with the outward selective dissolution of Al and inward precipitation of Ce-hydroxide. Due to this "two-way road" dynamics, the area above IMPs in the interior of the Ce-rich deposit is

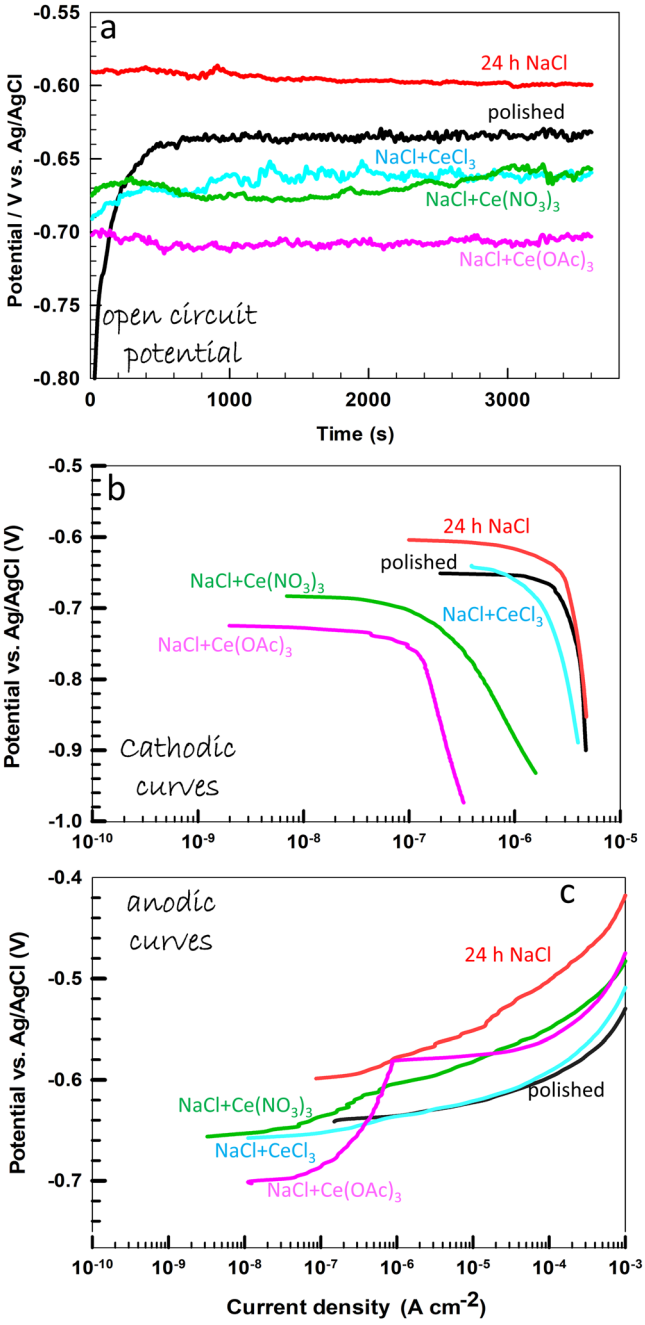

Figure 19. Electrochemical measurements recorded in 0.1 M NaCl on freshly polished AA7075-T6 sample (not pre-immersed) and AA7075-T6 samples pre-immersed for 24 h in 0.1 M NaCl, 0.1 M NaCl + 3 mM $CeCl_3$, 0.1 M NaCl + 3 mM $Ce(NO_3)_3$, and 0.1 M NaCl + 3 mM $Ce(OAc)_3$. (a) dependence of the open circuit potential on stabilization time and potentiodynamic polarization curves recorded separately in (b) cathodic and (c) anodic direction from the stabilized E_{oc}. The scan rate was 1 mV s^{-1}. Current densities at selected potentials −0.75 V and −0.60 V are given in Table V. Representative measurements were given in the figures, while all the repetitions are presented in Figs. S7 and S8.

complex comprising: (i) a mixed Cu-rich/Al-depleted interface layer which contains Fe, some O, and also Cl right on top of IMP, (ii) an intermediate mixed Ce-Cu-Al-Fe layer with smaller contents of Cu and Fe than in inner layer and larger content of O; the intermediate layer is overtopped with (iii) a mixed Ce-Al-hydroxide layer making the vast interior of the deposited dome. Large deposits were not exclusively Ce-hydroxide but incorporated Al and also some Cl.

At the matrix, the chloride-assisted dealloying mechanism was not operative. Instead, a few nanometre thick Al-oxide was overtopped with up to 100 nm thick Ce-hydroxide. The difference in thickness of the Ce-conversion layer was 50–100 times less than on large IMPs.

The action of Ce(III) acetate differs entirely from that of Ce(III) chloride and nitrate. No big Ce-rich deposits on the IMPs or matrix surface were observed. Instead, the whole surface was covered by a thin layer of Ce-hydroxide which prevented the selective dealloying of IMPs, including the S-phase.

Ce-conversion layers formed during 24 h immersion in NaCl with added Ce-salts affected the electrochemical properties, as measured in 0.1 M NaCl solution separately for anodic and cathodic branches. The reduction of both cathodic and anodic activities depended on the type of Ce salt used following the order: chloride < nitrate < acetate, with corrosion potential progressively shifting more negative. The Ce-conversion layer formed from Ce(III) acetate salt assured the highest degree of protection of the underlying 7075-T6 substrate because it strongly mitigates the selective dealloying of the IMP. This study verifies that the process of Ce-deposition from the aqueous solution is complex based on the dynamics of dealloying intermetallic particles.

Acknowledgments

The financial support by Slovenian Research Agency is acknowledged (grants No. P2–0393 and P1–0134). The authors also acknowledge the Centre of Excellence on Nanoscience and Nanotechnology - Nanocenter, Ljubljana, Slovenia to access the scientific equipment (FIB/SEM/EDS).

ORCID

Ingrid Milošev https://orcid.org/0000-0002-7633-9954
Peter Rodič https://orcid.org/0000-0001-8664-0129

References

1. B. R. W. Hinton, D. R. Arnott, and N. E. Ryan, *Met. Forum*, **7**, 211 (1984).
2. D. R. Arnott, N. E. Ryan, B. R. W. Hinton, B. A. Sexton, and A. E. Hughes, *Appl. Surf. Sci.*, **22/23**, 236 (1985).
3. A. J. Aldykewicz Jr, H. S. Isaacs, and A. J. Davenport, *J. Electrochem. Soc.*, **142**, 3342 (1995).
4. L. Paussa, F. Andreatta, N. C. Rosero Navarro, A. Durán, and L. Fedrizzi, *Electrochim. Acta*, **70**, 25 (2012).
5. F. H. Scholes, C. Soste, A. E. Hughes, S. G. Hardin, and P. R. Curtis, *Appl. Surf. Sci.*, **253**, 1770 (2006).
6. I. Milošev, A. Kraš, and P. Rodič, to be submitted.
7. T. G. Harvey, *Corr. Eng. Sci. Techol.*, **48**, 248 (2013).
8. A. Kolics, A. S. Besing, P. Baradlai, and A. Wieckowski, *J. Electrochem. Soc.*, **150**, B512 (2003).
9. L. Paussa, F. Andreatta, D. De Felicis, E. Bemporad, and L. Fedrizzi, *Corros. Sci.*, **78**, 215 (2014).
10. K. A. Yasakau, M. L. Zheludkevich, S. V. Lamaka, and M. G. S. Ferreira, *J. Phys. Chem. B*, **110**, 5515 (2006).
11. S. B. Brachetti-Sibaja, M. A. Domínguez-Crespo, A. M. Torres-Huerta, W. de la Cruz-Hernández, and E. Onofre-Bustamante, *J. Electrochem. Soc.*, **159**, C40 (2012).
12. E. A. Matter, S. Kozhukharov, M. Machkova, and V. Kozhukharov, *Corros. Sci.*, **62**, 22 (2012).
13. T. A. Markley, M. Forsyth, and A. E. Hughes, *Electrochim. Acta*, **52**, 4024 (2007).
14. H. Shi, E.-H. Han, and F. Liu, *Corros. Sci.*, **53**, 2374 (2011).
15. J.-A. Hill, T. Markley, M. Forsyth, P. C. Howlett, and B. R. W. Hinton, *J. Alloy Compd.*, **509**, 1683 (2011).
16. P. Rodič and I. Milošev, *J. Electrochem. Soc.*, **163**, C85 (2016).
17. I. Milošev and P. Rodič, *Corrosion*, **72**, 1021 (2016).
18. B. Volarič and I. Milošev, *Corr. Eng. Sci. Techol.*, **52**, 201 (2017).
19. P. Rodič, I. Milošev, M. Lekka, F. Andreatta, and L. Fedrizzi, *Electrochim. Acta*, **308**, 337 (2019).
20. I. Milošev and P. Rodič, *J. Electrochem. Soc.*, **169**, 011504 (2022).
21. D. Marunkić, J. Pejić, B. Jegdić, S. Linić, J. Perišić, B. Radojković, and A. Mariković, *J. Electrochem. Soc.*, **168**, 081501 (2021).
22. F. Andreatta, M.-E. Druart, A. Lanzutti, M. Lekka, D. Cossement, M.-G. Olivier, and L. Fedrizzi, *Corros. Sci.*, **65**, 376 (2012).
23. R. G. Buchheit, R. P. Grant, P. F. Hlava, B. Mckenzie, and G. L. Zender, *J. Electrochem. Soc.*, **144**, 2621 (1997).
24. R. G. Buchheit, M. A. Martinez, and L. P. Montez, *J. Electrochem. Soc.*, **147**, 119 (2000).

25. Y. Zhu, K. Sun, and G. S. Frankel, *J. Electrochem. Soc.*, **165**, C807 (2018).
26. M. Olgiati, P. J. Denissen, and S. J. Garcia, *Corros. Sci.*, **192**, 109836 (2021).
27. A. Kosari, F. Tichelaar, P. Visser, H. Zandbergen, H. Terryn, and J. M. C. Mol, *Corros. Sci.*, **177**, 108947 (2020).
28. A. Kosari, H. Zandbergen, F. Tichelaar, P. Visser, P. Taheri, H. Terryn, and J. M. C. Mol, *Corros. Sci.*, **177**, 108912 (2020).
29. Y. Zhu, K. Sun, J. Garves, L. G. Bland, J. Locke, J. Allison, and G. S. Frankel, *Electrochim. Acta*, **319**, 634 (2019).
30. F.-L. Zeng, Z.-L. Wei, J.-F. Li, C.-X. Li, X. Tan, Z. Zhang, and Z.-Q. Zheng, *Trans. Nonferrous Met. Soc. China*, **21**, 2559 (2011).
31. A. Kosari, M. Ahmadi, F. Tichelaar, P. Visser, Y. Gonzales-Garcia, H. Zandbergen, H. Terryn, and J. M. C. Mol, *J. Electrochem. Soc.*, **168**, 041505 (2021).
32. S. Sainis, S. Roşoiu, E. Ghassemali, and C. Zanella, *Surf. Coat. Technol.*, **402**, 126502 (2020).
33. A. E. Hughes, C. MacRae, N. Wilson, A. Torpy, T. H. Muster, and A. M. Glenn, *Surf. Interface Anal.*, **42**, 334 (2010).
34. G. O. Ilevbare, O. Schneider, R. G. Kelly, and J. R. Scully, *J. Electrochem. Soc.*, **151**, B453 (2004).
35. I. Milošev, B. Kapun, and P. Rodič, *to be submitted J. Electrochem. Soc*.
36. Q. Meng and G. S. Frankel, *J. Electrochem. Soc.*, **151**, B271 (2004).
37. N. Birbilis and R. G. Buchheit, *J. Electrochem. Soc.*, **155**, C117 (2008).
38. A. E. Hughes, A. Boag, A. M. Glenn, D. McCulloch, T. H. Muster, C. Ryan, C. Luo, X. Zhou, and G. E. Thompson, *Corros. Sci.*, **53**, 27 (2011).
39. M. Bethencourt, F. J. Botana, M. J. Cano, M. Marcos, J. M. Sánchez-Amaya, and L. Gonzáles-Rovira, *Corros. Sci.*, **51**, 518 (2009).
40. B. Volarič, A. Mazare, S. Virtanen, and I. Milošev, *Corrosion*, **76**, 18 (2020).